Computers and Fluids 275 (2024) 106248

Contents lists available at ScienceDirect

Computers and Fluids

journal homepage: www.elsevier.com/locate/compfluid

Adjacency-based, non-intrusive model reduction for vortex-induced vibrations

Leonidas Gkimisis [a,*], Thomas Richter [b], Peter Benner [a,b]

[a] Max Planck Institute for Dynamics of Complex Technical Systems, Computational Methods in Systems and Control Theory (CSC), Sandtorstraße 1, 39106 Magdeburg, Germany

[b] Otto-von-Guericke-Universität Magdeburg, Faculty of Mathematics, Institute for Analysis and Numerics, Universitätsplatz 2, 39106 Magdeburg, Germany

ARTICLE INFO

Dataset link: https://github.com/lgkimisis/VIV_sFOM_POD_inference

MSC:
76D05

Keywords:
Non-intrusive model reduction
Vortex-induced vibrations
Fluid–structure interactions

ABSTRACT

Vortex-induced Vibrations (VIV) pose computationally expensive problems of high practical interest to several engineering fields. In this work we develop a non-intrusive, reduced-order modeling methodology, applied to two-dimensional (2D), VIV cases subject to a laminar, incompressible flow. Performing a physics-informed approximation of the Arbitrary Lagrangian–Eulerian (ALE) incompressible Navier–Stokes (NS), we derive a discrete-time, quadratic-bilinear model structure for the velocity flowfield on a reference domain. This structure, along with a predefined sparsity pattern motivated by the adjacency-based sparsity of the discretized NS-ALE operators, leads to the formulation of a sparse, full-order model (sFOM) inference problem. Thus, the data-driven inference task requires solving many "local" least squares (LS) problems, isolating the contribution of geometrically "nearest neighbours" for each degree of freedom. Numerical aspects of inference such as data centering and regularization, as well as the direct enforcement of boundary conditions under the sFOM formulation are extensively discussed. The inferred, sFOM operators are then projected to a non-intrusive reduced-order model (ROM) for the velocity flowfield via the Proper Orthogonal Decomposition (POD). The resulting non-intrusive ROM (sFOM-POD) is coupled with the first-principle, 2D solid oscillation equations, resulting to a hybrid physics-informed/first-principle VIV dynamics model, simulated using an implicit time integration scheme. The mapping of the coupled solution from the ALE reference domain to the current configuration is also presented. This methodology is applied to two testcases of an elliptical, non-deformable solid mounted on springs, subject to $Re = 90,180$ flows. Numerical results indicate a successful coupling between the data-driven flowfield and solid dynamics, with prediction errors of less than 3% for both the flowfield and the solid oscillation. A comparative study with respect to the sFOM-POD dimension indicates the robustness and potential of the approach.

1. Introduction

Vortex-induced Vibrations (VIV) comprise a class of Fluid-Structure Interaction (FSI) problems with high practical interest to numerous engineering fields, among which are wind, offshore and aerospace engineering [1,2]. The system dynamics concern a two-way coupled response of a non-deformable solid body mounted on elastic supports, subject to a fluid flow. A multitude of complex dynamical phenomena arise from the interplay between solid and fluid dynamics, through the mechanism of asymmetric vortex shedding in the wake of the solid body [3]. Vortex shedding patterns, as well as solid-fluid coupling mechanisms greatly vary, depending on the flow conditions and solid properties of a given configuration [4,5].

In practice, the dynamically varying loads resulting from vortex shedding can lead to strong vibrations and thus a significant decrease in structure fatigue life. Such vibrations could be proven particularly destructive in applications such as underwater pipelines [6], turbine poles [7] or structural cables [8] and are thus carefully accounted for during engineering design. Apart from VIV suppression, intensive research is being performed on efficient harnessing of the kinetic energy of vortex-induced vibrations for energy production [9,10]. Both these fields indicate the strong motivation in developing efficient VIV simulation tools for engineering design, optimization and control.

Over the past decades, a number of methods have been developed for the direct numerical simulation of FSI and VIV problems [11–13], confronting issues such as numerical stability and computational overhead [14,15]. Concise reviews of numerical methods for FSI problems are given in [16,17]. Nonetheless, even for the regime of incompressible, laminar flows, the two-way coupling of two high-dimensional

* Corresponding author.
E-mail address: gkimisis@mpi-magdeburg.mpg.de (L. Gkimisis).

https://doi.org/10.1016/j.compfluid.2024.106248
Received 10 March 2023; Received in revised form 5 March 2024; Accepted 13 March 2024
Available online 15 March 2024

subsystems (i.e. a CFD and a structural finite element model) remains a challenging task. Depending on the problem at hand and the employed numerical solution, stability is not always guaranteed [18], while the stiff coupling and high dimensionality introduce a significant computational cost [14].

The growing field of model order reduction (MOR) comprises a potential alternative to bridge the gap between accuracy and computational overhead. MOR methods have proven to be efficient for several demanding, high-dimensional fluid and solid dynamics applications, leveraging computational cost and accuracy [19–22]. A number of research works have also been presented for different FSI aspects and applications. Notably, Liberge et al. employed POD to the flow around an oscillating cylinder, transferring the FSI problem to a global, fixed domain [23]. Using experimental Particle Image Velocimetry (PIV) data, Riches et al. [24] also employed POD, to investigate the intrinsic mechanisms of VIV wake-dynamics. A reduced basis method differentiating between solid, fluid and deformation modes for intrusive model reduction was developed by Nonino et al. applied to both partitioned and monolithic FSI models [25]. Focusing on parameter-dependent problems, Benner et al. proposed a low-rank method to increase the Newton iteration's computational efficiency for FSI computations [26]. In a high-Reynolds regime, Lieu et al. produced a POD-based model for the aeroelastic response of a complete F-16 aircraft, interpolating the model response over varying free-stream Mach numbers [27].

In cases where only simulation or experimental data are available, non-intrusive model reduction methods are being employed for modeling and prediction purposes. Depending on the availability of data and the prediction goal, there are input–output and state-access approaches. In the first category, only input–output data are available. In the context of FSI, Poussot-Vassal et al. [28] used the Loewner framework for the prediction of aircraft response to gust forcing, while Dai et al. developed a Recurrent Neural Network architecture for the non-intrusive prediction of pitching airfoil dynamics [29], focusing on the phenomenon of stall flutter. In cases where state measurements are possible, as in the case of commercial software simulations or PIV campaigns [30], one aims to infer the dynamics of the complete system. In that direction, Zastrow et al. [31] presented results on one-way coupled aeroelastic flutter using the method of Operator Inference, while Xiao et al. [32] presented a non-intrusive reduced-order model for FSI problems, based on radial basis function interpolation over time. In a slightly different direction, Yao et al. [33] focused on VIV problems at low Reynolds numbers, proposing a linear, Eigenvector Realization Algorithm approach to investigate the mechanism of transition to vortex shedding for different VIV configurations. In this study, we focus on dynamical predictions on laminar, low mass ratio, 2-dimensional VIV testcases [34,35], by proposing a novel, non-intrusive, ROM methodology.

In further detail, we present a methodology for physics-informed, data-driven model reduction, focusing on the prediction of 2D laminar, vortex-induced vibration dynamics. The approach assumes state access to the flow velocity fields, to infer the coupled flow/solid dynamics response. A non-intrusive model for the incompressible fluid flow is constructed on an ALE reference configuration. To account for the grid deformation, the velocity data are being interpolated to a reference domain through an ALE map, given by the solution of a Laplace equation. We show that the structure of the NS-ALE formulation for the velocity flowfield is approximately quadratic-bilinear. Motivated by the adjacency-based sparsity of the discretized NS-ALE operators, we propose a novel method to construct a full-order, sparse, non-intrusive model (sFOM) for the velocity flowfield, with an a priori adjacency-based, sparsity pattern. To that end, we locally infer the operators by solving one LS problem for each internal degree of freedom (DOF) with an L_2 regularization term. A proper treatment of the DOFs on the domain boundary allows for a direct enforcement of the Dirichlet boundary conditions at the fluid inlet and the fluid/solid interface on the sFOM level. By projecting onto a POD basis, the resulting non-intrusive ROM (sFOM–POD) for the fluid subsystem is then coupled with the first-principle solid motion oscillations and solved implicitly in time. The map to the deformed configuration is also considered as a post-processing step of the VIV predictions. The proposed methodology is showcased for two VIV cases of an oscillating solid along the streamwise and transverse directions, subject to a $Re = 90$ and a $Re = 180$ flow, respectively. Through these testcases, the predictive capabilities as well as several properties of the proposed approach are highlighted.

The rest of this work is structured in the following way: A review of the theoretical background on vortex-induced vibrations is given in Section 2, motivating the non-intrusive model formulation for the velocity flowfield. The developed methodology is analyzed in Section 3, for the construction of a non-intrusive fluid dynamics ROM and its coupling with the solid oscillations along the transverse and streamwise directions. Finally, the model is tested for two testcases of $Re = 90$ and $Re = 180$ flows past an ellipse-shaped body, with corresponding results given in Section 4. Conclusions and potential future work is discussed in Section 5.

2. Theoretical background

In this section, we present the physical modeling for laminar, vortex-induced vibration problems, which motivates the structure of the developed non-intrusive, data-driven model for the fluid velocity field.

2.1. Vortex-induced vibrations

As schematically depicted in Fig. 1, the problem consists of an incompressible fluid flow over a non-deformable body that can oscillate along the streamwise and transverse (x and y) directions. The equations of motion for the solid (s) displacement $\mathbf{d}_s$ are

$$\rho_s A_s \partial_{tt} \mathbf{d}_s + K\mathbf{d}_s = (\rho_s - \rho_f) A_s \vec{g} - \int_{\partial S} \boldsymbol{\sigma}(\mathbf{u}, p)\vec{n}\, \mathrm{d}\partial S, \tag{1}$$

where $\vec{n}$ is the unit normal vector on ∂S pointing from the solid to the fluid and K is a diagonal matrix with the spring constants k_x, k_y. The cross-sectional area of the solid is A_s, the solid and fluid densities are ρ_s and ρ_f respectively and σ is the 2-dimensional fluid stress tensor.

The integral term of (1) encodes the dynamic coupling condition between the fluid and solid subsystems. Hence, the solid motion equations are essentially two uncoupled, externally forced oscillations. We neglect internal damping to promote vortex-induced vibrations [2].

For the fluid flow, we focus on the regime of 2D incompressible, laminar flows

$$\nabla \cdot \mathbf{u} = 0, \quad \rho_f(\partial_t \mathbf{u} + (\mathbf{u}\cdot\nabla)\mathbf{u}) = \nabla\cdot\boldsymbol{\sigma} + \rho_f \vec{g}, \tag{2}$$

with velocity $\mathbf{u}$, pressure p, kinematic viscosity ν_f, gravity acceleration $\vec{g}$ and density ρ_f. The stress tensor σ for a Newtonian fluid is:

$$\boldsymbol{\sigma} = \rho_f \nu_f (\nabla\mathbf{u} + \nabla\mathbf{u}^T) - p\mathbb{I}, \tag{3}$$

where $\mathbb{I}$ is an appropriate identity operator. The imposed boundary conditions to the flow are the kinematic coupling condition at the fluid/solid interface, the velocity at the inlet and the "do-nothing" condition at the outlet ($x = l$) [14], given below

$$\begin{cases} \mathbf{u} = \partial_t \mathbf{d}_s \ at\ \Omega(t) \cap S, \\ \mathbf{u} = \mathbf{u}_{in} \ at\ x = 0, \\ \nu_f \nabla\mathbf{u}\cdot\mathbf{n} - p\mathbb{I} = 0 \ at\ x = l \end{cases}. \tag{4}$$

From the Eulerian perspective, the fluid domain $\Omega(t)$ is changing over time (see Fig. 1). Through the ALE framework [17], the NS are mapped to a reference domain $\hat{\Omega}$, which could be selected to be the domain configuration at $t = 0$. The map from the reference domain to the current configuration is then: $\hat{\mathbf{x}} \mapsto \mathbf{x} = \hat{\mathbf{x}} + \hat{\mathbf{d}}(t)$. The deformation

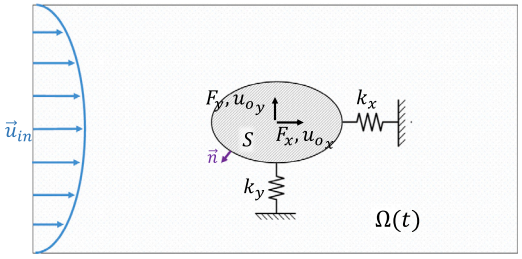

Fig. 1. Problem schematic representation: A non-deformable body with translational degrees of freedom along x, y, subject to an incompressible channel flow.

field of the current configuration with respect to the reference one is given through function $\hat{\mathbf{d}}(t)$ (ALE map). In cases where small grid deformations are encountered, the ALE map $\hat{\mathbf{d}}(t)$ can be computed by solving a Laplace problem. However, for larger deformations necessary modifications should be made to avoid degeneracy of mesh elements. For an analytical discussion of possible definitions of the ALE map, the reader is directed to Section 5.3.5 of [14]. In this study, we limit ourselves to a Laplacian ALE map for moderate grid deformations:

$$-\operatorname{div}\left(\hat{\nabla}\hat{\mathbf{d}}\right) = \mathbf{0} \quad \text{in } \hat{\Omega}\times(0,T], \tag{5}$$

with boundary conditions on the interface $\hat{\Omega}\cap S$, and on the domain external boundaries:

$$\begin{cases} \hat{\mathbf{d}}(t) = \mathbf{d}_s(t) - \mathbf{d}_s(0) \text{ on } \hat{\Omega}\cap S \\ \hat{\mathbf{d}}(t) = \mathbf{0} \text{ on domain bounds.} \end{cases} \tag{6}$$

We notice that using definition (5), the only time dependence of the ALE map originates from the boundary conditions (6) and that $\hat{\mathbf{d}}$ depends solely on the solid deformation $\mathbf{d}_s(t)$. This observation will be proven useful in the ROM level, since the ALE map can be computed at a low cost. Denoting F as the Jacobian of the ALE map, and $J = \det F$, we get a NS-ALE formulation [14,25]:

$$\begin{cases} \rho_f J\left(\partial_t\hat{\mathbf{u}} + \hat{\nabla}\hat{\mathbf{u}}\mathbf{F}^{-1}\left(\hat{\mathbf{u}} - \partial_t\hat{\mathbf{d}}\right)\right) - \hat{\nabla}\cdot\left(J\hat{\sigma}\left(\hat{\mathbf{u}},\hat{p}\right)\mathbf{F}^{-T}\right) = J\rho_f\vec{g} \\ \hat{\nabla}\cdot\left(J\mathbf{F}^{-1}\hat{\mathbf{u}}\right) = 0 \end{cases}, \tag{7}$$

where

$$\mathbf{F} = \mathbb{I} + \partial_{\mathbf{x}}\hat{\mathbf{d}},\ J = det(\mathbf{F}). \tag{8}$$

From the model reduction point of view, following a different approach from [23], we are interested in constructing the fluid dynamics model on domain $\hat{\Omega}$. In this way, we isolate the flowfield snapshots from the solid motion, thus avoiding typical issues of transport-dominated equations projection [36] close to the FSI interface. The ALE formulation (7) of the NS equations is fitting this approach. However, the corresponding structure of the equations is no longer quadratic, as in typical, fixed domain NS [37]. Instead, the structure of (7) exhibits further nonlinearities, due to the Jacobian of the ALE map (8).

At this point, we show that under certain assumptions on the system response, the NS-ALE structure can be approximated by a set of quadratic-bilinear ordinary differential equations (ODEs). We will employ this physics-informed structure to infer a non-intrusive model for the flowfield in VIV problems. In particular, using a smooth ALE map as (5) and considering small-amplitude oscillations, we can approximate $F \approx \mathbb{I}$ (and thus $J \approx 1$). A more detailed illustration of this simplification, based on dimensional arguments, is made in Appendix A. The link of this assumption with the assumption of small deformations made for (5) is also discussed. Based on the above, (7) is simplified to

$$\begin{cases} \rho_f\left(\partial_t\hat{\mathbf{u}} + \hat{\nabla}\hat{\mathbf{u}}\left(\hat{\mathbf{u}} - \partial_t\hat{\mathbf{d}}\right)\right) - \hat{\nabla}\cdot\left(\hat{\sigma}\left(\hat{\mathbf{u}},\hat{p}\right)\right) = \mathbf{0} & \text{in } \hat{\Omega}\times(0,T] \\ \hat{\nabla}\cdot\left(\hat{\mathbf{u}}\right) = 0 & \text{in } \hat{\Omega}\times(0,T] \end{cases}, \tag{9}$$

where gravity forces are neglected, since their relative magnitude is negligible (e.g. Section 6.6, [14]). The pressure can be computed by taking the divergence of (9):

$$-\hat{\Delta}\hat{p} = \rho_f\hat{\nabla}\cdot\hat{\nabla}\hat{\mathbf{u}}\left(\hat{\mathbf{u}} - \partial_t\hat{\mathbf{d}}\right) \tag{10}$$

The structure of (9), as well as the algebraic link between velocity and pressure (10) will comprise the foundation towards the flowfield physics-informed, data-driven model.

3. Methodology

3.1. Physics-informed, data-driven flowfield model

Making the assumption of small displacements, the pressure Eq. (10) is substituted to (9). Discretizing Eq. (9) in space, a physics-informed, quadratic-bilinear structure for the evolution of the velocity flowfield $\mathbf{u} \in \mathcal{R}^{2n\times 1}$ is obtained, where n is the number of discretized mesh nodes. Based on the approximation of small displacements, this physics-informed, quadratic-bilinear system of equations for the velocity flowfield is derived in Appendix B. We hereby only present the final, approximate model structure for the flowfield velocities on a reference domain $\hat{\Omega}$, which will be used for the non-intrusive model inference

$$\begin{aligned} \mathbf{u}^{k+1} = {} & A_u\mathbf{u}^k + H_u\left(\mathbf{u}^{k+1}\otimes\mathbf{u}^{k+1}\right) + K_u\left(\partial_t\mathbf{d}_s^{k+1}\otimes\mathbf{u}^{k+1}\right) \\ & + B\,\partial_t\mathbf{d}_s^{k+1} + L\,\mathbf{u}_{in}^{k+1}, \end{aligned} \tag{11}$$

with sparse operators A_u, H_u, K_u and a priori known operators L, B for the enforcement of the Dirichlet boundary conditions at the flow inlet and the fluid-solid interface. Notation $\hat{}$ has been dropped, since, in the following we focus on the velocity flowfield on the reference configuration. An implicit coupling of the fluid and solid subsystems is required, since computation of $\mathbf{u}^{k+1}$ requires $\partial_t\mathbf{d}_s^{k+1}$. To this end, we will couple a non-intrusive model for the flowfield with the first-principle model governing the oscillatory motion of the non-deformable solid in (1). This is analytically discussed in Section 3.7.

3.2. Average flowfield removal

We hereby make a note on the decomposition of the flow into a dynamical and a stationary, average flowfield. For the flow around an oscillating cylinder, the mean flowfield $\bar{\mathbf{u}}$ over the reference domain $\hat{\Omega}$ is omnipresent and includes a significant part of the flow energy. To showcase this property, we use data from the second of the two numerical testcases, later presented in Section 4. The case corresponds to a $Re = 180$ VIV case for a channel geometry as in Fig. 1, on a mesh of 10256 nodes. The timeseries includes 1000 timesteps of $\Delta t = 0.01$, over which the flow develops and forms a Kármán vortex street.

In Fig. 2, the singular values of the 10256×1000 flowfield snapshot matrix are plotted for velocity components u_x and u_y, before and after removing the corresponding time series average ($\bar{u}_x$ and $\bar{u}_y$). Note that the main difference for the singular values of the u_x and $\tilde{u}_x = u_x - \bar{u}_x$ data matrices is visible for the respective maximum singular values σ_1 and $\tilde{\sigma}_1$. This suggests that the first singular vector of the u_x data matrix basically contains the main information of the time-averaged flow $\bar{u}_x$. In order to verify this, we plot the first SVD mode of u_x in Fig. 3a. The maximum error between $\bar{u}_x$ and the rank-1 reprojection of the u_x data onto the first singular vector is given in Fig. 3b. The error values of less than 1% validate that the first singular vector of the u_x dataset is indeed closely linked to $\bar{u}_x$. This effect is less pronounced for the u_y component, since modes linked to vortex shedding encode a significant portion of the u_y flowfield energy. Observing the difference between the singular values of u_y and $\tilde{u}_y = u_y - \bar{u}_y$ in Fig. 2 and the corresponding singular vectors, we conclude that the average $\bar{u}_y$ is more closely related to the third singular vector of the u_y dataset. The third singular vector of u_y is plotted in Fig. 3b and indeed qualitatively matches the expected time series average $\bar{u}_y$. The error between $\bar{u}_y$ and the rank-1 reprojection

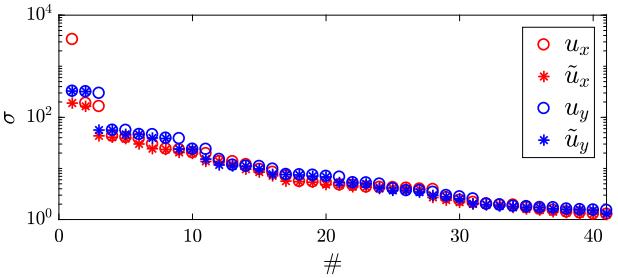

Fig. 2. Singular value decomposition of 10256 × 1000 data matrices of the u_x, u_y velocity components of the 2D flowfield for the later presented, Re = 180 VIV case (Section 4). The first singular vector of u_x is linked to $\overline{u_x}$.

of the u_y data onto the third SVD mode in Fig. 3d shows a maximum missmatch of ≈ 10%.

As a result, we write the velocity field as:

$$\mathbf{u}(t) = \bar{\mathbf{u}} + \tilde{\mathbf{u}}(t). \tag{12}$$

Excluding the mean $\bar{\mathbf{u}}$ is known to be beneficial [38] for the numerical manipulation of the data, since it reduces the condition number of the corresponding data matrix (see Fig. 2). Thus, assuming we have state access over some training time $[0, T_1]$, we subtract the time-average velocity field from the data and infer the dynamics of the $\tilde{\mathbf{u}}(t)$ component. From this point and on, we refer to the prediction of $\tilde{\mathbf{u}}(t)$, dropping the $\tilde{}$ notation for simplicity. Subtracting $\bar{\mathbf{u}}$ by substituting (12) in (13) leaves the prescribed sparse, quadratic-bilinear structure unchanged, introducing only an additional bias term, C. This is extensively discussed in Appendix B. The structure of the equations becomes

$$\begin{aligned}\mathbf{u}^{k+1} \;=\; & A\mathbf{u}^{k} + H\left(\mathbf{u}^{k+1}\otimes\mathbf{u}^{k+1}\right) + K\;\left(\partial_t \mathbf{d}_s^{k+1}\otimes\mathbf{u}^{k+1}\right) \\ & + B\;\partial_t \mathbf{d}_s^{k+1} + L\;\mathbf{u}_{in}^{k+1} + C.\end{aligned} \tag{13}$$

3.3. Grid deformation

Model (13) encodes the physics-informed structure of the moderately-deformed domain, incompressible NS-ALE formulation in (9). Thus, it corresponds to the flow solution on a reference configuration. Before examining the solution of (13) for the reference configuration, we need to complement the model with an ALE map from the reference domain to the current, deformed one.

For the non-intrusive modeling procedure, the flow velocity data over some training time $t = [0, T_1]$ is imported, on a given grid $\Omega(t)$. The grid adjacency information is needed for the application of the aforementioned adjacency-based sparsity pattern.

The deformation of the grid over $[0, T_1]$ is often provided along with velocity and pressure data, in case of proprietary software. However, different solvers employ variations of (5) to derive the grid deformation [14,25], often not traceable by the end-user. Also, in the case of experimental data (e.g. PIV campaigns [38]) there is no notion of grid deformation. In either case, we need to ensure that the same ALE map is defined and used for both training and testing time intervals of the non-intrusive model.

To achieve this, it is necessary to construct a fluid mesh on which the imported data will be interpolated and select an ALE map (in our case (5)). Hence, the imported velocity data are interpolated at each training timestep from the current configuration of the solver mesh (or e.g. PIV domain in experimental campaigns), to the current configuration of the new mesh, given the selected ALE map. For the constructed mesh, grid adjacency information is stored, allowing for the application of an adjacency-based sparsity pattern in the non-intrusive model.

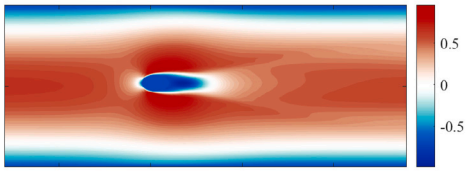

(a) 1st singular vector for u_x (scaled): Subtracting the average flowfield $\bar{u}_x$ from the data is closely linked to removing this singular vector/value and reduces the data matrix condition number.

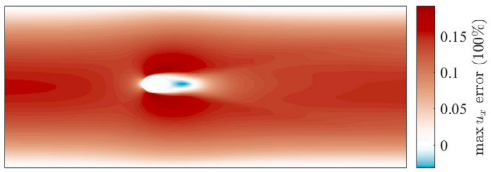

(b) Maximum error between the average flowfield $\bar{u}_x$ and the rank-1 reprojected flowfield onto the first u_x SVD mode (percentage given with respect to max(u_x) = 2.77 m/s).

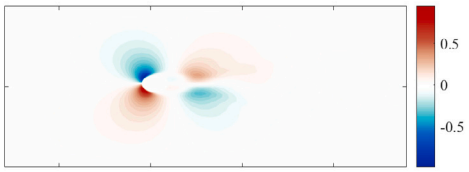

(c) 3rd singular vector for u_y (scaled): Subtracting the average flowfield $\bar{u}_y$ from the data is linked to removing the 3rd singular vector from the u_y SVD.

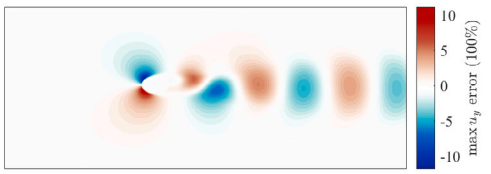

(d) Maximum error between the average flowfield $\bar{u}_y$ and the rank-1 reprojected flowfield onto the third u_y SVD mode (percentage given with respect to max(u_y) = 1.38 m/s). The energy contribution of the first three u_y SVD modes is comparable (see Figure 2).

Fig. 3. Link between the 1st u_x and 3rd u_y singular modes to the average flowfields $\bar{u}_x$ and $\bar{u}_y$, respectively.

The motion of each grid node is given by discretizing and solving (5). We have denoted the discretized Laplace operator, augmented by necessary identity matrix rows for the Dirichlet boundary conditions in (6), with Λ. The corresponding system of equations is then

$$\Lambda\hat{\mathbf{d}} = [\mathbf{0}\;\mathbf{d}_s(t) - \mathbf{d}_s(0)]^T \tag{14}$$

with a right-hand side of zeros for all internal nodes of $\hat{\Omega}$. FS denotes the set of nodes on the interface $\Omega(t) \cap S$, which should follow the motion of the solid (see Eq. (6)). After inverting matrix Λ and considering the non-zero right-hand side for nodes FS, the displacement of the grid nodes is given by

$$\hat{\mathbf{d}} = \left(\sum_{i \in FS} \Lambda^{-1}_{:,i} \right) (\mathbf{d}_s(t) - \mathbf{d}_s(0))^T, \tag{15}$$

where the reference configuration is taken as the one at $t = 0$. We observe that $\left(\sum_{i \in FS} \Lambda^{-1}_{:,i} \right)$ should be computed once. Grid deformation can then be computed for any given solid displacement $\mathbf{d}_s(t)$. In essence, (15) gives an analytical expression of a basis for the grid displacement $\hat{\mathbf{d}}$ with respect to the solid displacement [25].

3.4. Non-intrusive, sparse full-order model (sFOM) inference

The task in physics-informed, non-intrusive modeling is to infer the unknown operators of the prescribed structure in (13), i.e. to construct a physics-informed, data-driven model for the 2D velocity field. Several non-intrusive model reduction approaches infer dense model operators directly in a space of reduced dimension, by first projecting the data to the leading SVD modes of the snapshot matrix [20,21]. We hereby follow a different approach, motivated by the discussed adjacency-based sparsity of the discretized operators of the full-order model [39,40].

The idea of inferring full-order, sparse operators from discretized ODEs and partial differential equations (PDEs) was investigated in [40,41] from the perspective of numerical stencil inference for both linear and nonlinear problems. In [39], the enforcement of physics-informed sparsity was showcased for a linear advection example, while [42] investigated a similar problem in the context of compressed sensing. In this work, the idea of adjacency-based sparsity is generalized to the context of physics-informed inference for a sparse, full-order model (sFOM) in (13) for the VIV flowfield dynamics. Employing such an approach is also accommodated by the critical role of mesh motion and corresponding grid generation need in FSI problems, already discussed in Section 3.3. Thus, in a non-intrusive modeling context, we aim to exploit grid adjacency information to identify geometrically adjacent nodes for each DOF and extract corresponding velocity data. In this manner, we fix a sparsity pattern for the sFOM operators. A LS problem can then be formulated for the inference of the sparse full-order operators, based on the physics-informed model structure in (13).

Enforcing sparsity enables inferring full-order, data-driven operators in (13), since only adjacent node products of terms $K\left(\partial_t \mathbf{d}_s \otimes \mathbf{u}^{k+1}\right)$ and $H\left(\mathbf{u}^k \otimes \mathbf{u}^k\right)$ are assumed to be non-zero. This also allows enforcing uniqueness of the data-driven model in the full-order level, with respect to the states (velocities), by avoiding commutative velocity products on the quadratic term. This is a stronger constraint than the corresponding removal of commutative products on the quadratic term of a ROM.

In practice, we examine one row of (13) corresponding to some internal DOF, i. Since we focus on grid adjacency, we should note that for this 2D velocity field, there are two DOFs per mesh node. Thus, we denote by $q(i)$ the set of DOFs which correspond to mesh nodes, adjacent to the node of DOF i. Based on the aforementioned idea of adjacency-based sparsity, the dynamical model for DOF i depends only on the contribution of the set of DOFs $q(i)$.

Dirichlet boundary conditions for DOFs at $x = 0$ (i_{in}) and on $F \cap S$ (i_s) can be a priori satisfied by setting $A_{i_{in},:} = H_{i_{in},:} = K_{i_{in},:} = 0$, $C_{i_{in}} = 0$ and $A_{i_s,:} = H_{i_s,:} = K_{i_s,:} = 0$, $C_{i_s} = 0$, while entries of value 1 are registered in respective positions of B, L. We split the quadratic terms into two contributions h_A and h_B; the first one includes products including the velocity components of the examined node i, while the second one includes products between adjacent node velocities only. Based on this, we now look more closely into a row of (13). The equation for the u_x or u_y velocity of a node i with a set of adjacent DOFs $q(i)$ is then

$$u_i^{k+1} = \sum_{q(i)} \left(a_{i,j} u_j^k + \left[h_{A_{i,j}} \; h_{A_{i+zn,j}} \right] \left[u_i^{k+1} u_{i+zn}^{k+1} \right]^T u_j^{k+1} \right.$$
$$\left. + \left[k_{i,j} \; k_{i,j+2n} \right] u_j^{k+1} \partial_t \mathbf{d}_s + \sum_{q(i)} \left(h_{B_{j,l}} u_l^{k+1} u_j^{k+1} \right) \right), \tag{16}$$

where we set $z = 1$ for u_x ($1 \le i \le n$) and $z = -1$ for u_y ($n+1 \le i \le 2n$), respectively. In this general form, the terms of h_A, h_B are not unique. In practice, we eliminate the terms of h_B involving the velocity components of DOF i so that h_A and h_B share no common terms. We also eliminate non-unique, commutative terms in h_B. As a result, if DOF i has m adjacent DOFs, then h_{B_i} includes $\binom{m}{2}$ terms.

Eq. (16) for DOF i can be written for every timestep in $[0, T_1]$. This leads to a LS sFOM inference formulation, considering the ith row entries of operators A, H, K

$$\min_{a_{i,:}, h_{A_{i,:}}, h_{B_{i,:}}, k_{i,:}} \left\| \left[a_{i,:}, h_{A_{i,:}}, h_{B_{i,:}}, k_{i,:} \right]^T \mathcal{D} - \mathbf{u}_i^{k+1} \right\|_2, \tag{17}$$

where, following the notation of [37],

$$\mathcal{D}^T = \begin{bmatrix} \mathbf{u}_{q(i)} \\ \mathbf{u}_i \mathbf{u}_{q(i)} \\ \mathbf{u}_{i+nz} \mathbf{u}_{q(i)} \\ \mathbf{u}_{q(i)}^2 \\ \mathbf{u}_{q(i)} \otimes \mathbf{d}_s \end{bmatrix}. \tag{18}$$

The solution of (17) for an internal DOF i is a vector with the entries of the ith row for operators A, H, K. Based on grid adjacency information, these entries can then be stored in corresponding positions of the operators, thus leading to the adjacency-based sparsity pattern of the sFOM. It is evident that the aforementioned advantages of sFOM inference are leveraged by a significant increase in the offline cost of the approach. The solution of (17) scales with the number of DOFs on the interpolated grid and thus the corresponding computational overhead is expected to be significantly higher, compared to that of projection-first methods.

3.5. L_2 regularization

Adding regularization is required for the practical solution of (17), to avoid numerical errors due to small singular values of $\mathcal{D}$. We employ Tikhonov regularization to penalize solutions with high L_2 norm by modifying each LS problem as follows:

$$\min_{a_{i,:}, h_{A_{i,:}}, h_{B_{i,:}}, k_{i,:}} \left(\left\| \left[a_{i,:}, h_{A_{i,:}}, h_{B_{i,:}}, k_{i,:} \right]^T \mathcal{D} - \mathbf{u}_i^{k+1} \right\|_2 \right.$$
$$\left. + \lambda_1 \left\| \left[a_{i,:}, k_{i,:} \right] \right\|_2 + \lambda_2 \left\| \left[h_{A_{i,:}}, h_{B_{i,:}} \right] \right\|_2 \right). \tag{19}$$

Two distinct regularization terms are introduced, since the singular values of the quadratic terms in H scale differently than those of linear and bilinear terms in A and K [43,44]. For the current application, setting $\lambda_1 = \lambda_2$ yields satisfactory results. Hence, for each degree of freedom, we solve problem (19), for different values of $\lambda = \lambda_1 = \lambda_2$. The optimal regularization parameter is chosen based on the L-curve criterion [45]. In particular, we aim to leverage between the LS solution error and the solution norm. Denoting $\left\| \vec{b} \right\|_2$ as the LS solution error and $\left\| \vec{x} \right\|_2$ as the solution norm, we seek for

$$\min_{\lambda} \left(\left\| \hat{\vec{b}} \right\|_2^2 + \left\| \hat{\vec{x}} \right\|_2^2 \right), \tag{20}$$

where $\hat{}$ indicates normalization of the $\left\| \vec{b} \right\|_2$ and $\left\| \vec{x} \right\|_2$ values to $[0, 1]$. Fig. 4 illustrates the procedure of finding the optimal regularization parameter for the ith DOF: For each λ value, we obtain a pair $(\vec{b}, \vec{x})$. The λ value for which the corresponding pair (denoted $(\vec{b}_L, \vec{x}_L)$) satisfies (20) is then selected.

In the sFOM setting, we can reduce the computational cost by spatially interpolating the optimal LS regularization parameter. In essence, since velocity varies smoothly over the domain (dealing with an incompressible flow), matrix $\mathcal{D}$ in (24) and thus its singular values are also expected to vary smoothly over the domain. We can thus compute the optimal regularization parameter for a subset of the mesh nodes and

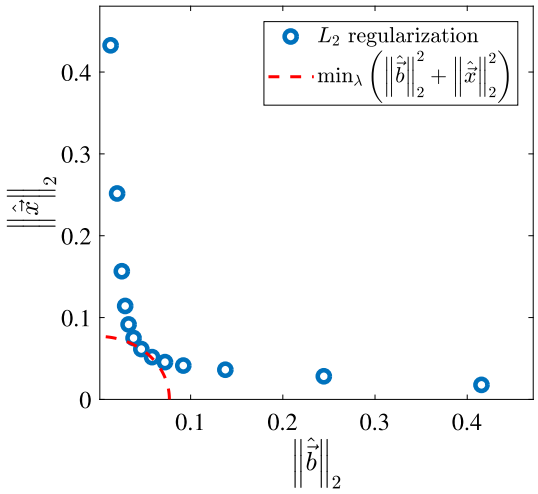

Fig. 4. Example of L_2 regularization L-curve criterion: The sFOM inference solution $\hat{\vec{x}}$ (and thus the λ value) which gives the smallest normalized distance from the $\left(\left\| \hat{\vec{b}} \right\|_2, \left\| \hat{\vec{x}} \right\|_2^2 \right)$ origin is chosen.

approximate λ at the remaining nodes by linear interpolation on the two-dimensional reference configuration.

For every λ value tested, we sum the solution norm $\|\vec{x}\|_2$ for each DOF i (i.e. for each row of Eq. (13)) to get the Frobenius norm of the inferred operators. Similarly, for every λ, we sum the error $\left\| \vec{b} \right\|_2$ over i and get the overall L_2 error of the inferred model with this regularization parameter. By doing so for each of the λ values, we can plot a global L-curve for the inferred model. The corresponding sums over i for the optimal λ (after solving Eq. (19) at each DOF) are calculated. These correspond to the sFOM training error and sFOM operators norm. The sFOM training error and operators norm will not necessarily lie on the global L-curve, since an optimal λ value is computed for each LS problem in Eq. (19).

Fig. 5 indicates the trade-off between the non-intrusive model training error and inferred operators norm, for the $Re = 180$ testcase, further analyzed in Section 4. By spatial interpolation of the regularization parameter, for both u_x and u_y fields, the LS solution computational cost is significantly reduced. For example, if 20 λ values are considered and the optimal λ is computed for 10% of the DOFs, then only one LS problem should be solved for the remaining 90% of the DOFs. This translates to a decrease in the involved LS computational cost by a factor of ≈ 6.5 (without considering the cost of λ interpolation). A zoomed-in view of the global L-curve is depicted in Fig. 5a. A minor increase in the sFOM training error when interpolating λ is recorded, compared to the sFOM computed from solving (19) for all degrees of freedom. Fig. 5b illustrates the optimal regularization parameter for each grid node based on (20), for the u_x velocity component. We observe that λ is higher in the wake region of the flow, where the flow exhibits more complex dynamics. Fig. 5c corresponds to the interpolated λ case, computing the optimal parameter for 10% of the internal grid nodes. Fig. 5b and Fig. 5c exhibit differences on the selected λ, however the resulting difference in training error is only minor. It is noted that parallelization of the LS problems could also significantly reduce the offline clock time required for inferring the operators through the employed methodology. However, this has not been considered in this work.

At this step, the sFOM (13) has been computed. Next, the force induced from the flow to the solid should be predicted, as to couple the fluid and solid dynamics.

3.6. Surface forces modeling

As shown in (1), the forcing from the fluid flow to the solid motion originates from the integral of stresses on the body surface (Eq. (3)).

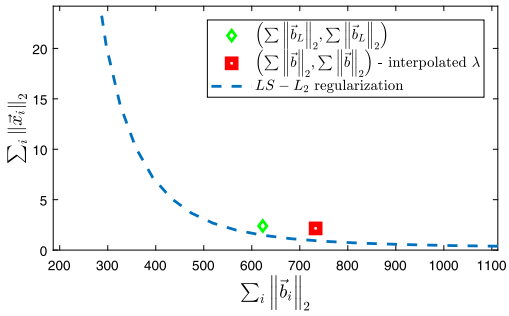

(a) L-curve for the DOF-wise and interpolated λ sFOM: Slightly increased error for the interpolated λ model, at a significantly lower cost.

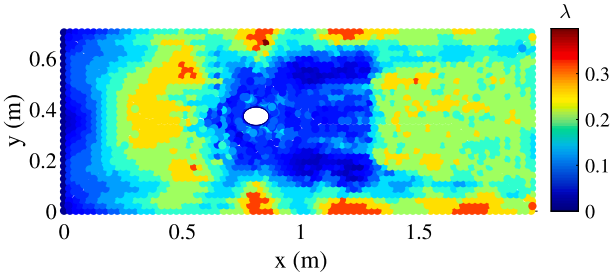

(b) Optimal λ computed at each grid node (u_x velocity).

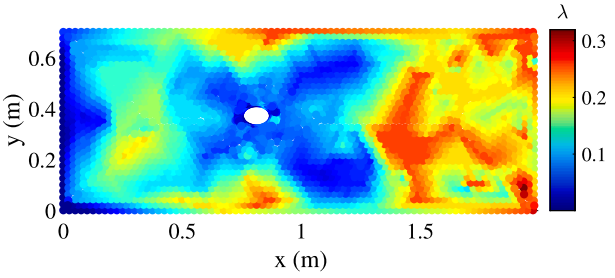

(c) Optimal λ computed at 10% of grid nodes, interpolated for the rest 90%.

Fig. 5. Regularization parameter selection for fluid nodes: Indicatory example for a $Re = 180$ dataset (discussed in detail in Section 4). Increased λ values in the flow wake for both the exact and the interpolated optimal regularization strategies.

Focusing on non-deformable solid motion along the two axes, a model for the forces F_x, F_y (Fig. 1) is required. The mean velocity flowfield over the training time $[0, T_1]$ results in a constant force $\bar{\mathbf{F}} = \left[\bar{F}_x, \bar{F}_y\right]^T$. As a result, we can similarly write the force as

$$\mathbf{F} = \bar{\mathbf{F}} + \tilde{\mathbf{F}}. \tag{21}$$

We aim to predict the dynamically evolving component $\tilde{\mathbf{F}}$, in line with the focus on the dynamically varying velocity flowfield component. In the following we drop $\tilde{}$ for simplicity.

We assume solid motion parameters (mass, spring constants) to be known. Mass and (linear) spring constants can be easily determined both numerically, but also experimentally through the impulse response for the solid oscillation. Therefore, only kinematic data is necessary for constructing the non-intrusive model. The velocity training data for the solid, as well as the known mass and spring constants are substituted in (1) to obtain numerical training data for the integral forcing terms we aim to predict.

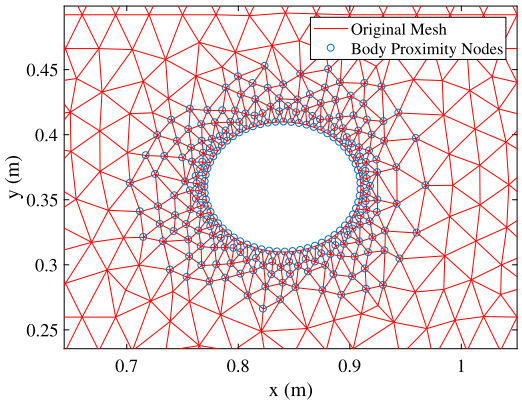

Fig. 6. Body-proximity nodes: Given a normal distance threshold from the interface $\hat{\Omega} \cap S$, only $2n_F$ DOFs are included in the body forces non-intrusive model. This threshold is empirically set to contain the flow boundary layer and thus scaling with the boundary layer thickness $\sim \frac{1}{\sqrt{Re}}$ could be suitable.

The force $\mathbf{F}$ corresponds to the oscillation forcing term $\int_{\partial S} \boldsymbol{\sigma}(\mathbf{u}, p)\vec{n}\, \mathrm{d}\partial S$ in Eq. (1). Based on Eq. (3), the flow-induced forcing would correspond to a linear, viscous term, and a pressure term. We model the pressure forcing as a quadratic model, by neglecting the contribution of bilinear terms in Eq. (10). Thus, we hereby employ a quadratic sFOM for the force, in the following form:

$$\mathbf{F}^k = A_F \mathbf{u}^k + H_F \left(\mathbf{u}^k \otimes \mathbf{u}^k\right). \tag{22}$$

For this part, a second adjacency matrix is formulated. We make the assumption that only the velocity of nodes sufficiently close to the body will contribute to the force acting on it. As before, this is motivated by the approximate sparsity of the inverse of the laplacian in Eq. (10), and the integral of Eq. (3) in Eq. (1). As a result, the output sFOM (22) has $2n_F$ DOFs (velocities u_x and u_y), where $n_F \ll n$ is the number of nodes at the proximity of the reference interface $\hat{\Omega} \cap S$, given some normal distance threshold. An illustration of this proximity grid is given in Fig. 6.

Not all $\binom{2n_F}{2}$ terms of $\mathbf{u} \otimes \mathbf{u}$ were included in the force model, but only the ones corresponding to adjacent pairs of DOFs. In fact, using only quadratic terms of the sort $u_i u_{q_F(i)}$, where $q_F(i)$ denotes the adjacent DOFs within the proximity grid, for each DOF i, was found to be sufficient for body forces prediction, while restricting the involved least square problem dimension.

As presented for the velocity flowfield in 3.4 and 3.5, we infer the sparse, full-order matrices A_F, H_F by solving an L_2-regularized LS problem

$$\min_{A_F, H_F} \left(\left\| \begin{bmatrix} A_F & H_F \end{bmatrix}^T \mathcal{D}_F - \mathbf{F} \right\|_2 + \lambda_F \left\| \begin{bmatrix} A_F & H_F \end{bmatrix} \right\|_2 \right), \tag{23}$$

where A_F, H_F are of dimension $2 \times 2n_F$. The optimal λ_F is found as before through an L-curve, with $\mathcal{D}_F$ given by

$$\mathcal{D}_F^T = \begin{bmatrix} \mathbf{u}_{q_F(i)} \\ \mathbf{u}_i \mathbf{u}_{q_F(i)} \end{bmatrix}. \tag{24}$$

3.7. Coupled sFOM − POD-oscillation dynamics

Up to this point, the sFOM for the velocity flowfield and the force on the solid have been computed. The non-intrusive ROM (denoted as sFOM−POD) is then computed via projection, using a POD basis on the reference configuration $\hat{\Omega}$ [46].

The flowfield model is projected to the leading singular modes of data matrix U. The columns of U are vectorized velocity data over the fluid mesh (see 3.3), stacked over training time $[0, T_1]$. Following the logic of POD, we compute the SVD $U = \Phi \Sigma \Psi^T$ and truncate the leading r singular values. Denoting $\Phi_r = \Phi_{:,1:r}$, we project the grid velocity $\mathbf{u}^k$ to the leading r modes, such that

$$\mathbf{u}^k = \Phi_r \tilde{\mathbf{u}}^k. \tag{25}$$

Applying (25) to model (13), we obtain the sFOM−POD operators as follows:

$$\begin{aligned} \tilde{A} = \Phi_r^T A \Phi_r,\ \tilde{H} = \Phi_r^T H \left(\Phi_r \otimes \Phi_r\right),\ \tilde{K} = \Phi_r^T K \left(I_{2\times 2} \otimes \Phi_r\right), \\ \tilde{B} = \Phi_r^T B,\ \tilde{L} = \Phi_r^T L,\ \tilde{C} = \Phi_r^T C. \end{aligned} \tag{26}$$

We observe that due to the sparsity of matrix H, we can efficiently compute the projected operator $\tilde{H}$. In particular, we split matrix H into H_A with entries including the "self node" terms (see Eq. (16)) and H_B containing unique products of adjacent node velocities. We store only the non-trivial entries of these two matrices; as a result, we need to store matrices of dimensions $2n \times 2\max_i q(i)$ and $2n \times \binom{2(\max_i q(i)-1)}{2}$, respectively for H_A and H_B, where n is the total number of nodes. This allows using a different computational stencil for each of the two terms H_A and H_B. In this application, we use second-degree adjacent nodes ("adjacent nodes of adjacent nodes", or $q(q(i))$) for H_A and first-degree adjacent nodes for H_B, limiting the number of required Kronecker products. Since the two matrices share no common non-zero entries, we can then write

$$H \left(\Phi_r \otimes \Phi_r\right) = H_A \left(\Phi_r \otimes \Phi_r\right) + H_B \left(\Phi_r \otimes \Phi_r\right). \tag{27}$$

Knowing the sparsity pattern of H_A and H_B, we compute only the relevant Kronecker products of $\Phi_r \otimes \Phi_r$ for each case. Once matrix $H \left(\Phi_r \otimes \Phi_r\right)$ is computed by the above procedure, it is multiplied on the left with Φ_r^T. This procedure significantly reduces the number of operations required for the projection of the quadratic matrix.

For the force acting from the flow to the solid, we follow a similar procedure: We identify the lines of Φ_r corresponding to the nodes close to the body from the grid adjacency information (as shown in Fig. 6). We denote Φ_s the $2n_F \times r$ matrix by retaining the necessary lines of Φ_r. Then, the projection step for (22) is

$$\tilde{A}_F = A_F \Phi_s,\ \tilde{H}_F = H_F \left(\Phi_s \otimes \Phi_s\right). \tag{28}$$

Having constructed the sFOM−POD for both the velocity field and the resulting forces on the solid along the streamwise and transverse direction, we are ready to couple the fluid (data-driven) model with the solid (first-principle) one. The sFOM−POD writes as

$$\begin{cases} \tilde{\mathbf{u}}^k = \tilde{A}\tilde{\mathbf{u}}^{k-1} + \tilde{H}\left(\tilde{\mathbf{u}}^k \otimes \tilde{\mathbf{u}}^k\right) + \tilde{K}\left(\partial_t \mathbf{d}_\mathbf{s}^k \otimes \tilde{\mathbf{u}}^k\right) + \tilde{B}\partial_t \mathbf{d}_\mathbf{s}^k + \tilde{L}\mathbf{u}_{in} + \tilde{C} \\ \mathbf{F}^k = \tilde{A}_F \tilde{\mathbf{u}}^k + \tilde{H}_F \left(\tilde{\mathbf{u}}^k \otimes \tilde{\mathbf{u}}^k\right), \end{cases} \tag{29}$$

while the solid oscillation Eqs. (1) are integrated using a Crank-Nicholson scheme, with timestep Δt:

$$\begin{cases} \partial_t \mathbf{d}_\mathbf{s}^k + \frac{\Delta t K}{2\rho_s A_s} \mathbf{d}_\mathbf{s}^k - \frac{\Delta t}{2} \mathbf{F}^k = \partial_t \mathbf{d}_\mathbf{s}^{k-1} - \frac{\Delta t K}{2\rho_s A_s} \mathbf{d}_\mathbf{s}^{k-1} + \Delta t\, \mathbf{g} + \frac{\Delta t}{2} \mathbf{F}^{k-1} \\ \mathbf{d}_\mathbf{s}^k - \frac{\Delta t}{2} \partial_t \mathbf{d}_\mathbf{s}^k = \mathbf{d}_\mathbf{s}^{k-1} + \frac{\Delta t}{2} \partial_t \mathbf{d}_\mathbf{s}^{k-1} \end{cases} \tag{30}$$

An interesting observation during simulation was that the known stiff coupling between the fluid and solid subsystems in FSI numerical simulation [47,48] transfers also to this data-driven/first principle two-way coupling, rendering an explicit model unstable. Thus, the model is constructed with an implicit formulation, requiring convergence at each timestep. In detail, the force $\mathbf{F}^k$ resulting from the sFOM−POD prediction in $\tilde{\mathbf{u}}^k$ is driving the solid oscillation. The resulting solid displacement $\mathbf{d}_\mathbf{s}^k$ is in turn affecting the surrounding flow $\tilde{\mathbf{u}}^k$. A combined convergence criterion of $\left\|\tilde{\mathbf{u}}_{j+1}^k - \tilde{\mathbf{u}}_j^k\right\|_2 < res_1$ and $\left\|\mathbf{d}_{\mathbf{s}_{j+1}}^k - \mathbf{d}_{\mathbf{s}_j}^k\right\|_2 < res_2$ was used, where j denotes the index of iterations within timestep k. For each implicit iteration, a typical successive under-relaxation method was used [18].

Table 1
VIV simulation properties: Two testcases with $Re = 90, 180$ were examined, at a low mass ratio $\rho_s/\rho = 1.2$.

ν (m^2/s)	ρ (kg/m^3)	ρ_s (kg/m^3)	R_x (m)	R_y (m)
0.001	1	1.2	0.07	0.05
k_x (N/m)	k_y (N/m)	$\bar{u}_{in}$ (m/s)	Δt	
10	10	0.75/1.5	0.01	

4. Simulation results

4.1. VIV testcases and non-intrusive modeling setup

The above methodology was coded in MATLAB and applied to two numerical testcases for the VIV of an ellipse-shaped solid, with horizontal and vertical semiaxes R_x and R_y. Both numerical simulations were performed with the Gascoigne open-source, FSI solver [49] on a computational grid of 10256 nodes. The NS-ALE formulation (7) is solved for the fluid dynamics subsystem and a Laplacian ALE map is employed. Simulation time is 13.5 and 10 seconds respectively for $Re = 90,\ 180$.

The details for the two testcases are given in Table 1. The solid has streamwise and transverse eigenfrequencies (in vacuum) of $f_s = 4.38$ Hz and is subject to a laminar, incompressible channel flow. A parabolic velocity profile is prescribed at the channel inlet, with a maximum velocity of $u_{max} = 1.5\bar{u}_{in}$, while the domain size is 4×1 m^2. The reference length is twice the average of the semiaxes $D = R_x + R_y$ and the reference velocity u_∞ is the average inlet velocity. The two testcases then correspond to $Re = 90$ and $Re = 180$. A low mass ratio is also selected ($\rho_s/\rho = 1.2$), to promote a wide VIV lock-in velocity range and considerable peak amplitude [2]. The added mass is $m_A = 0.011$ kg, which leads to eigenfrequencies of the submerged solid of $f_N \approx 3.24$ Hz. The reduced velocity $U^* = u_\infty/(f_N D)$ in the two testcases is then $U^* = 1.93$ and $U^* = 3.86$. This indicates that they respectively belong to the lower and higher ends of the initial VIV branch ($U^* \lesssim 4.75$) [24]. This regime corresponds to a vortex shedding frequency f_v, higher than the solid eigenfrequency f_N. As f_v increases (linearly with u_∞), the amplitude of VIV oscillations increase, reaching a maximum at $f_v/f_N \approx 1$.

The grid interpolation step described in 3.3 was performed focusing on a region close to the body. An unstructured mesh of $n = 3893$ nodes was constructed via Delaunay triangulation on a truncated domain of $[0.5, 2.6] \times [0.05, 0.95]$, with the use of the MESH2D MATLAB tool [50]. The data of the last 5.9 s of simulation were used in both cases, including a transient response. For the sFOM inference (19), regularization optimization was performed for 10% of the $2n$ DOFs, using 20 λ values on a logarithmic scale of $\lambda \in [10^{-4},\ 0.5]$. A similar procedure was performed for the force sFOM (23), considering nodes n_F within an ellipse of $1.5R_x,\ 1.5R_y$. 63% of the available time series was used as training data, based on which the sFOM was trained and the basis Φ_r was constructed. After the projection, the coupled model (29) and (30) was simulated using a successive under-relaxation parameter $\omega = 0.5$ [18]. For both testcases, a maximum of $4 - 5$ iterations per timestep were required to reach convergence. VIV predictions beyond the training time were then examined and the accuracy of the sFOM-POD was evaluated.

4.2. Velocity flowfield POD basis

Before presenting the ROM predictions, it is interesting to examine the POD basis onto which the sFOM for the velocity flowfield is projected (see Section 3.7). We will hereby focus on selected pairs of spatial and temporal SVD vectors Φ_i and Ψ_i of the two examined cases, which illustrate three significant mechanisms in VIV dynamics. This analysis will help to interpret the simulation results obtained with our approach in Sections 4.3 and 4.4, as well as provide insight into the projection step of Section 3.7 and the main mechanisms of VIV dynamics. For a detailed study focused on the POD of experimental VIV data, the reader is directed to [24].

After removing the data average (see Section 3.2), the first POD mode pair corresponds to convective vortex shedding for both $Re = 90$ and $Re = 180$. This is similar to the case of the flow over a cylinder [51], with this mode pair containing more than 50 % of the total kinetic energy of the flow. We hereby show only the first mode for $Re = 90$, u_x and u_y (Fig. 7a,b), since the second mode is just shifted by one quarter of the spatial wavelength. For a Strouhal number of $St = 0.21$ and choosing a reference velocity as $u_{max} = 1.13$ m/s, the expected vortex shedding frequency is close to $f_v \approx 1.97$ Hz. This is in relatively good accordance with the peak at 1.72 Hz of the Fourier spectrum of the temporal vector Ψ_1, given in Fig. 7c.

A mode that could be correlated with the slow-drift of the mean flow is also detected in both datasets. This mode (Φ_5 for $Re = 90$) captures the energy of flow transition to a limit-cycle behavior and is illustrated in Fig. 8 for both velocity components. The unresolved, low-frequency dynamics in the Fourier spectrum of Fig. 8c also hint towards a link of this mode with the slow-drift of the mean flow, while two minor peaks are noticed close to the vortex shedding and solid natural frequencies. The significance of such a mode depends on the presence of transient dynamics in the VIV simulation dataset and in many cases is individually treated [24].

In the case of $Re = 90$, other POD modes correspond mainly to multiples of the vortex-shedding frequency and corresponding wavelengths, since the solid forcing frequency is sufficiently below $f_N = 3.24$ Hz. However, in the case of $Re = 180$, the two frequencies $(f_v,\ f_N)$ are very close. This is specifically evident in Φ_5 of the corresponding basis, shown in Fig. 9. The Fourier transform of Ψ_5 (Fig. 9c) shows a strong peak at 3.12 Hz, indicating the presence of the solid natural frequency in the system dynamics. This is expected theoretically [2] for $Re = 180$ and can be captured by the ROM with more than 5 modes. It is noted that a departure from the exact value of $f_v/f_N = 1$ can be expected in cases of low mass ratio and damping [52], as the one considered here.

4.3. Solid oscillations

The oscillation velocity time series and corresponding sFOM-POD predictions are given in Fig. 10 for both testcases. The vertical dashed line indicates the end of the training time. From that point and on, the model predictions are tested against unseen simulation data. In both cases, the streamwise oscillation amplitude (along x) is more than one order of magnitude lower compared to the amplitude of the transverse oscillation. Furthermore, the transverse oscillations dominating frequency ($f \approx 1.72$ Hz for $Re = 90$) is half than that of streamwise motion, as theoretically expected.

For the case of $Re = 90$, the oscillations exhibit a very low amplitude (Fig. 10b), hinting a link to the lower end of the initial VIV branch [34]. On the contrary, the $Re = 180$ case shows strong transverse oscillations (Fig. 10d), almost one order of magnitude higher than that for $Re = 90$, often exhibited in the higher end of the initial VIV branch. Due to the vicinity of f_N and f_v, beating phenomena are observed for $Re = 180$ [53]. The coupled sFOM-POD-oscillation model captures the solid dynamics with high accuracy in both cases. It should be noted that VIV amplitude obtains a maximum value in the vicinity of $f_v/f_v \approx 1$ [2]. Hence, the results of Fig. 10 validate the "small deformation" approximation made for the physics-informed, non-intrusive model in Section 3, even for very low mass ratio VIV cases.

The qualitative differences in the transverse and streamwise oscillations are reflected on the ROM predictions error. The truncation of the SVD modes (25) leads to a corresponding truncation of the flow energy. If the VIV coupling is strong (as in the streamwise direction), even leading flow modes interact with the solid oscillation (see e.g. Fig. 9). However, in cases of weaker VIV coupling (as in Fig. 10a, c), it is

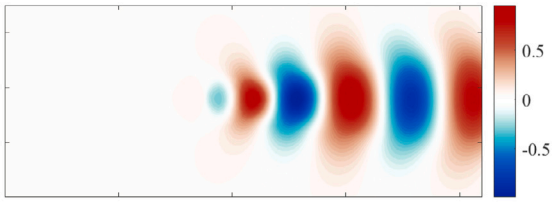

(a) Φ_1 for u_x velocity $(Re = 90)$

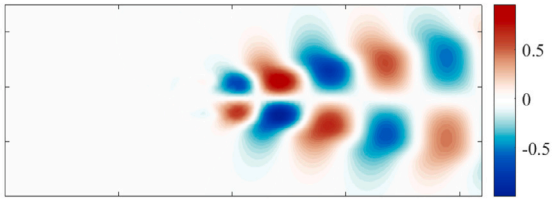

(b) Φ_1 for u_y velocity, $(Re = 90)$

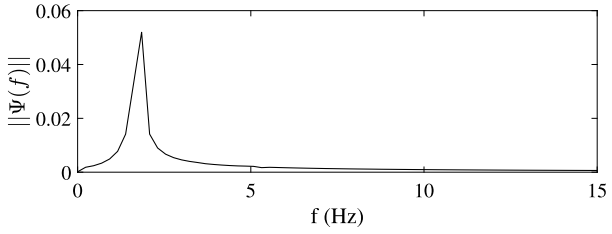

(c) Fourier spectrum of Ψ_1 $(Re = 90)$

Fig. 7. First POD mode for $Re = 90$: The first POD mode pair contains more than 50 % of the total kinetic energy of the flow (here only the first mode is displayed) and is linked with the 2S vortex shedding frequency (peak at $f = 1.72$ Hz). The values of $\boldsymbol{\Phi}_1$ are normalized to a $[-1, 1]$ scale for illustration purposes.

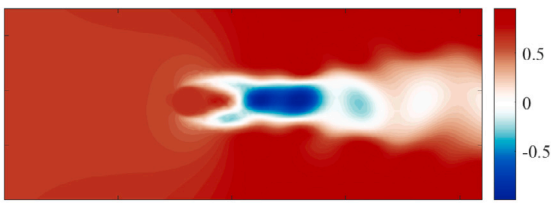

(a) Φ_5 for u_x velocity $(Re = 90)$

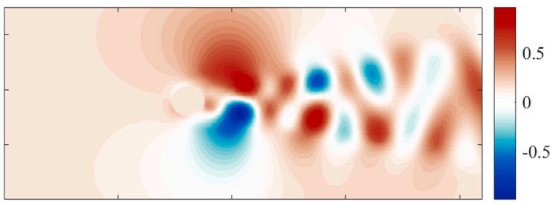

(b) Φ_5 for u_y velocity $(Re = 90)$

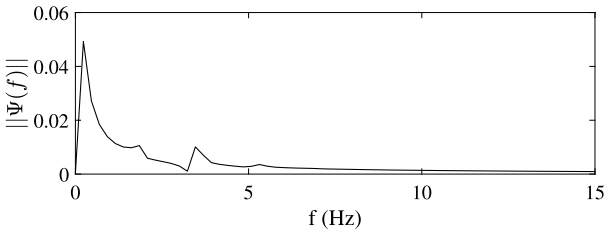

(c) Fourier spectrum of Ψ_5 $(Re = 90)$

Fig. 8. Fifth POD mode for $Re = 90$: A mode potentially linked to the slow-drift of the mean flow is captured, due to the transient wake dynamics. Minor peaks at f_v and f_N are observed.

likely that low energy modes that interact with the low-amplitude solid motion are truncated. Hence, the error for the $r = 30$ ROM prediction e.g. in Fig. 10c might seem relatively significant at specific times, however the corresponding ROM prediction error is negligible.

4.4. Flowfield predictions

For each simulation timestep, we can reconstruct the predicted velocity field in the reference configuration using (25). However, it is of interest to also map the reconstructed flowfield to the predicted current configuration. This can be done by using the dimensionless deformation field $\left(\sum_{i \in FS} \Lambda^{-1}_{:,i}\right)$ from (15) and multiplying with the predicted displacement of the solid body along both axes. The solution is then mapped to the predicted current configuration. This last step entrails a negligible added cost, since $\left(\sum_{i \in FS} \Lambda^{-1}_{:,i}\right)$ has been precomputed.

The CFD and predicted `sFOM-POD` flowfield for the final testing time is given in Figs. 11 and 12, for both velocity components of $Re = 90$. A corresponding comparison is given for $Re = 180$ in Figs. 13 and 14. The CFD solution indicates a 2S mode for both testcases, where two single vortices appear per oscillation cycle. This matches well-known results for laminar VIV with free body oscillations [2,34]. ROM predictions in both cases match the vortex dynamics qualitatively and quantitatively, using $r = 30$ modes. It is noted that the full-order numerical simulation (e.g. for $Re = 180$) requires approximately 40 minutes on a personal laptop. In contrast, the offline ROM cost corresponds to approximately 3 minutes, while the ROM numerical simulation requires just several seconds (for some typical ROM dimension of $\mathcal{O}(10)$).

We also compute an average, relative ROM error over the $\mathbf{u}_x$ and $\mathbf{u}_y$ flowfield, on the reference domain $\hat{\Omega}$. This reads (e.g. for the u_x component) as

$$e(t) = \frac{\|\mathbf{u}_{x_{CFD}} - \mathbf{u}_{x_{ROM}}\|_1}{n \ \max \mathbf{u}_{x_{CFD}}} \times 100\%. \tag{31}$$

Error e is recorded in Fig. 15 over time, for both testcases and both velocity components. For $Re = 180$, the error exhibits oscillations, possibly linked to both modeling and projection errors of the stronger vortex dynamics, compared to $Re = 90$. We observe that in the transient part of the data, the error reaches its peak value, approximately 1.5%. It is noted that the flowfield error originates from the combined effect of modeling and projection errors, as well as the error of coupling (29) with (30). In the testing time interval, the errors for $Re = 180$ (both u_x and u_y) oscillate for values below 1%. For $Re = 90$, the error shows a noticeable increase after the training time, reaching up to 2% at the end of the testing time. This is primarily linked with a phase shift, slightly noticeable in Fig. 10a. Transient dynamics induced by the slow, mean flow drift are not fully resolved during the training time (see the low-frequency peak in Fig. 9c). Thus, a gradual phase shift of the ROM predictions is observed during the testing time interval, leading to a respective, almost linear increase of the error in Fig. 15.

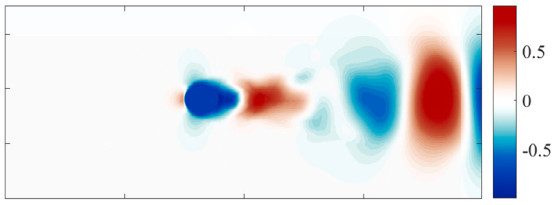

(a) Φ_5 for u_x velocity ($Re = 180$)

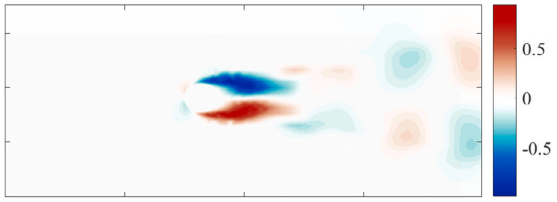

(b) Φ_5 for u_y velocity ($Re = 180$)

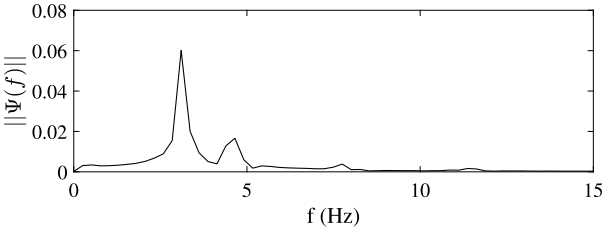

(c) Fourier spectrum of Ψ_5 ($Re = 180$)

Fig. 9. Fifth POD mode for $Re = 180$: Solid natural frequency affects the wake dynamics, since the case lies in the higher end of the initial VIV branch. A significant peak at 3.12 Hz, very close to the theoretical f_N value is observed in the Fourier spectrum of Ψ_5.

Finally, we perform a comparative study by averaging the error (31) over the testing time, with respect to the dimension r of the sFOM-POD ROM. As presented in Sections 3.4 and 3.7, the inferred sFOM is independent of the projection basis $\boldsymbol{\Phi}_r$ (Eq. (25)). After truncating the projection basis to 10 different r values, we simulate the resulting coupled system and record the average of error (31) from the end of training time T_1 to the final simulation time T. Fig. 16 illustrates the obtained results for both testcases and both velocity components. In the case of $Re = 180$, the resulting u_y error is slightly higher than u_x, especially for $r \leq 10$. For small values of r, the average error is higher for the $Re = 180$ case. That can be explained by the more rich dynamics exhibited for this case, as shown in Figs. 9 and 10c,d. Thus, comparably more POD modes are required to sufficiently capture the system dynamics. In both cases, the curve is flattened for a sFOM-POD dimension higher than 15, meaning that adding more POD modes does not provide any further information on the model dynamics [37]. From that r value and on, the underlying error made in (19) during sFOM inference is dominating the POD projection error. Fig. 16 also indicates a convergence of the ROM error to a certain value with increasing ROM dimension r. This property is typically acquainted in intrusive MOR (e.g. [25,27]), here inherited by the presented non-intrusive sFOM methodology. A similar error convergence behavior with the one observed for the non-intrusive model in Fig. 16 was reported for an intrusive FSI ROM in [25]. This indicates that the independence of the inferred sparse, full-order operators from the projection basis $\boldsymbol{\Phi}_r$ could result to an increased robustness of the non-intrusive ROM.

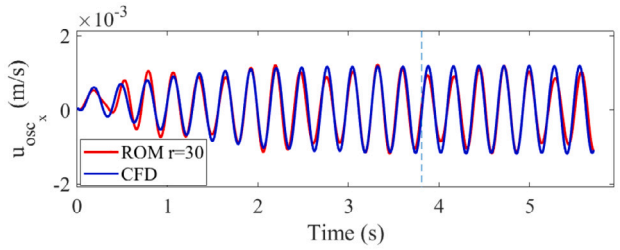

(a) Predictions for streamwise oscillation velocity, $Re = 90$.

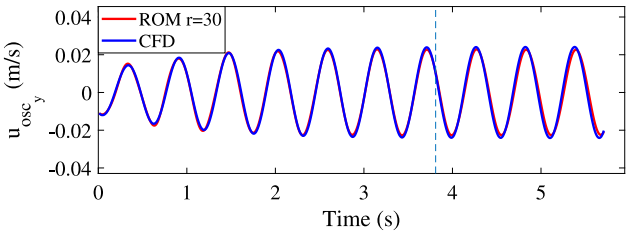

(b) Predictions for transverse oscillation velocity, $Re = 90$.

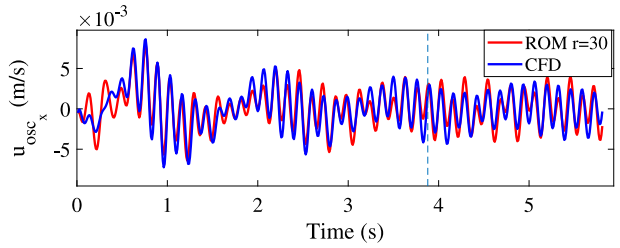

(c) Predictions for streamwise oscillation velocity, $Re = 180$.

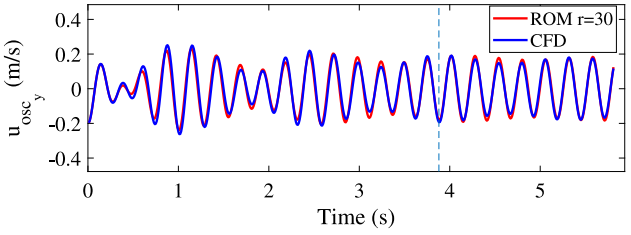

(d) Predictions for transverse oscillation velocity, $Re = 180$.

Fig. 10. Solid oscillations predictions: The coupled dynamics of the sFOM-POD flow ROM (29) and first-principle oscillation Eqs. (30) yield highly accurate predictions for the solid oscillations, capturing well the low-amplitude motion ($Re = 90$) as well as beating phenomena ($Re = 180$), even past the training time.

5. Outlook and future work

In this work, a non-intrusive model order reduction methodology was presented, applied to vortex-induced vibration problems. The dynamical model structure for the fluid velocity was motivated by the problem physics under the ALE formulation, while a physics-informed sparsity pattern was enforced through the grid adjacency information. An L_2 regularization term was added to the sFOM inference problem for each grid node velocity component and computational cost reduction strategies for the optimization of the regularization parameter were discussed. The physics-informed, data-driven velocity field ROM (sFOM-POD) was subsequently coupled with the first-principle solid oscillations and a method for mapping the reprojected solution from the reference to the deformed configuration was presented. Finally, the

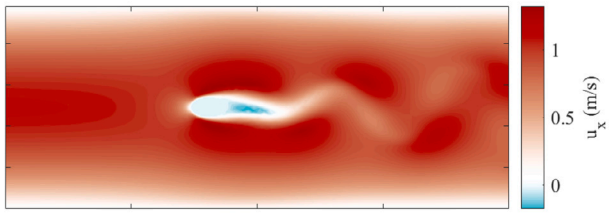

(a) CFD contour plot for u_x $(Re = 90)$

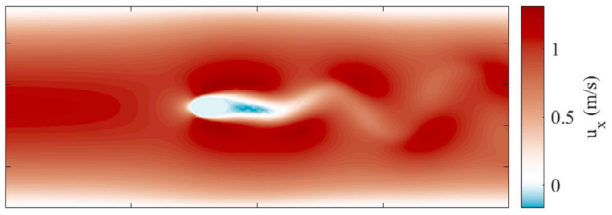

(b) sFOM-POD $(r = 30)$ contour plot for u_x $(Re = 90)$

Fig. 11. Contour plots at $t = 5.9$ s for the u_x flowfield at $Re = 90$: The non-intrusive model captures the 2S vortical mode as well as the flow features close to the oscillating body.

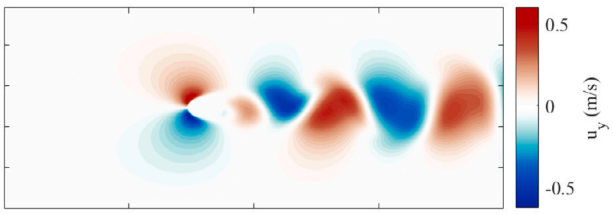

(a) CFD contour plot for u_y $(Re = 90)$

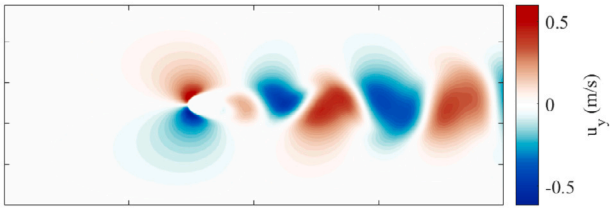

(b) sFOM-POD $(r = 30)$ contour plot for u_y $(Re = 90)$

Fig. 12. Contour plots at $t = 5.9$ s for the u_y flowfield at $Re = 90$: Slight phase mismatch, also indicated by the solid transverse oscillation prediction in Fig. 10b.

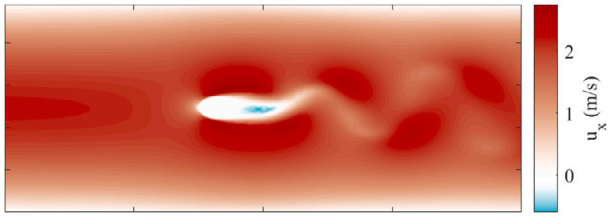

(a) CFD contour plot for u_x $(Re = 180)$

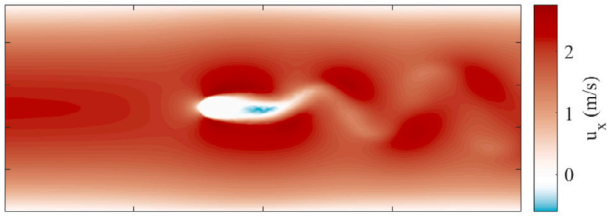

(b) sFOM-POD $(r = 30)$ contour plot for u_x $(Re = 180)$

Fig. 13. Contour plots at $t = 5.9$ s for the u_x flowfield at $Re = 180$: Accurate ROM prediction, with a double vortex shedding frequency compared to $Re = 90$.

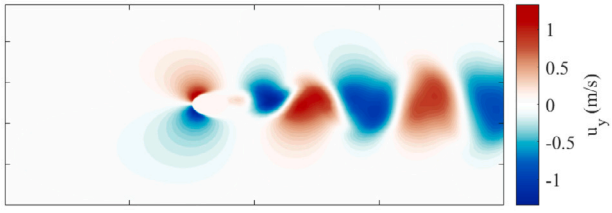

(a) CFD contour plot for u_y $(Re = 180)$

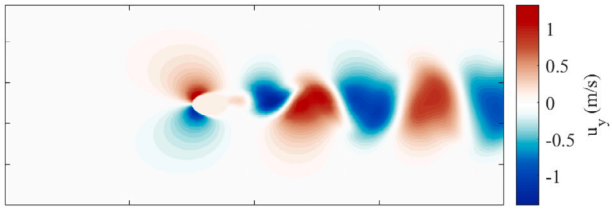

(b) sFOM-POD $(r = 30)$ contour plot for u_y $(Re = 180)$

Fig. 14. Contour plots at $t = 5.9$ s for the u_y flowfield at $Re = 180$: The non-intrusive model is again in good accordance with the corresponding CFD results at the end of testing time.

methodology was applied to two transient VIV testcases with $Re = 90$, $Re = 180$, which exhibit different VIV phenomena. Results on the prediction of both the solid oscillation and the surrounding flowfield with only 30 modes indicates the potential of the followed methodology; the solid oscillation was accurately predicted over the testing time interval, while the average velocity error over the domain was found to be less than 3%. Finally, a parametric study with respect to the sFOM-POD dimension showcased the increased ROM robustness offered by the inference of sparse, full-order operators.

The current work could comprise a first step towards a non-intrusive MOR framework for FSI problems. Hence, future work could incorporate several different aspects; in particular, the offline computational efficiency of the approach could be significantly enhanced. Potential approaches could include parallelization of the sFOM LS problems or domain segregation to regular sub-grids, where the local inference can be solved for only a small subset of the DOFs. Similarly, stability of the inferred sFOM prior to projection via POD should be investigated. On the application side, testing the developed non-intrusive ROMs under varying inputs and solid oscillation parameters would provide further insight on the attributes of the proposed methodology for VIV predictions. In a similar direction, the showcased sFOM independence from the SVD basis renders parametric MOR specifically interesting, aiming towards non-smooth parameter dependencies. Such studies could be performed for VIV problems with respect to different Reynolds

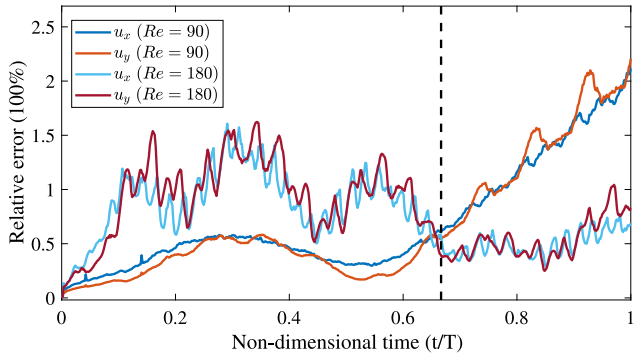

Fig. 15. Average error over the flowfield, for both u_x and u_y relative to $\max u_x$, $\max u_y$ over time.

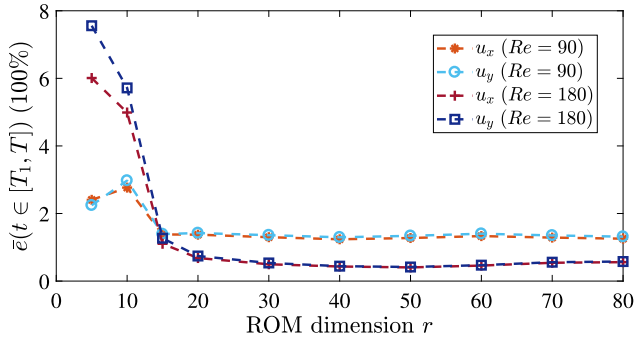

Fig. 16. Average error (31) over testing time, for different sFOM–POD dimensions r: A projection subspace dimension of [15, 20] is sufficient for the ROM, with an observed error convergence for a further r increase.

numbers, given the recorded rich coupled system dynamics and strong parametric dependence. Finally, the extension to deformable solids and consequently the formulation of a predictive, non-intrusive ROM methodology for FSI problems lies in the future scope of this work.

CRediT authorship contribution statement

Leonidas Gkimisis: Writing – original draft, Validation, Software, Methodology, Investigation, Conceptualization. **Thomas Richter:** Writing – review & editing, Supervision, Software, Resources, Methodology, Investigation, Conceptualization. **Peter Benner:** Writing – review & editing, Validation, Supervision, Resources, Methodology, Formal analysis, Conceptualization.

Declaration of competing interest

The authors declare that they have no known competing financial interests or personal relationships that could have appeared to influence the work reported in this paper.

Data availability

The data and MATLAB 2017 code used for this work are available in https://github.com/lgkimisis/VIV_sFOM_POD_inference.

Appendix A. Assumption of small deformations

A more detailed analysis of the approximation $F \approx \mathbb{I}$ and its link to the usage of ALE map (5) is hereby given, based on dimensional analysis.

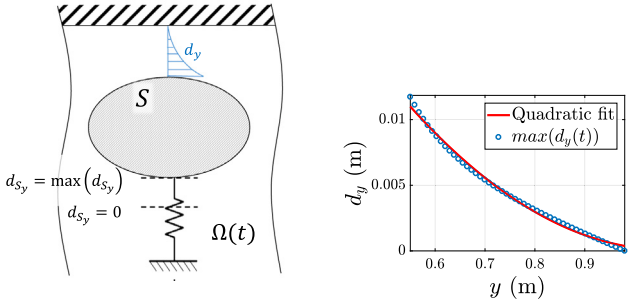

Fig. 17. Quantitative analysis of fluid displacement field. Left: Displacement d_y on vertical axis of symmetry of the flowfield, Right: Quadratic approximation for the displacement along the vertical symmetry axis.

Two-dimensional, laminar VIVs appear to be more severe in the transverse than in the streamwise direction [2] due to the mechanism of vortex shedding. Therefore, denoting $\hat{\mathbf{d}} = [d_x \; d_y]^T$:

$$d_x \approx 0.1 d_y \tag{32}$$

Our aim is to estimate the magnitude of the entries in $\partial_{\mathbf{x}}\hat{\mathbf{d}}$ compared to $\mathbb{I}$ in (8). For this reason, we focus on the grid displacements on the vertical axis of symmetry of the domain, where strong gradients are expected (due to the minimal distance from the channel wall and the smoothness of the solid surface — see Fig. 17). We consider a quadratic behavior of the transverse grid displacement d_y from the solid wall to the domain boundary, as shown in Fig. 17. This is a simple distribution that follows the simulation data well and allows to estimate the maximum value of $|\partial_y d_y|$.

By substituting the conditions on the interface $\Omega(t) \cap S$ and the wall ($d_y = 0$) to a quadratic fit for d_y, we can compute an estimate for the maximum absolute value of the gradient, $\max |\partial_y d_y|$, which will scale as

$$\mathcal{O}(max|\partial_y d_y|) \approx \frac{max(d_y)}{h}. \tag{33}$$

For the examined geometry, (33) gives an estimate in the order of $max|\partial_y d_y| \approx 10^{-2}$, considering that $h = 1m$ and $\mathcal{O}(max(d_y)) = 10^{-2}$ m. Based on the Laplacian ALE map (5), the second derivative of each displacement field (d_x, d_y) scales uniformly in both x and y directions. Thus, all entries in $\partial_{\mathbf{x}}\hat{\mathbf{d}}$ are expected to have a value in the order of $max|\partial_y d_y|$. As a result, we can estimate that the Frobenius norm of $\partial_{\mathbf{x}}\hat{\mathbf{d}}$ will also be in the order of $\approx 10^{-2}$, given (32). Based on the above dimensional arguments, it is expected that the validity of the approximation $F \approx \mathbb{I}$ will depend almost linearly on $max(d_y)/h$.

On the other hand, the validity of the chosen ALE map breaks down when it leads to degenerate mesh elements. This happens when the derivative J of the displacement gradient F (see (8)) approaches zero. Hence, the value of $max(d_y)/h$ for which the approximation $F \approx \mathbb{I}$ is invalid, is considerably lower that the value for which the ALE map will be invalid.

The preceding analysis for the validity of the derived physics-informed structure is only indicatory. It should be noted that the $F \approx \mathbb{I}$ approximation is made to reveal a physics-informed model structure. Since the data-driven solution is a LS fit to the data, the range of validity for the physics-informed model will differ from that of the corresponding PDE with the same approximation. Particularly, the LS solution could partially account for "unmodeled terms" by fitting the LS solution to the prescribed model structure accordingly. Although numerical results are encouraging, the effect of this approximation to possible over-fitting in cases of parametric non-intrusive modeling remains to be investigated.

Appendix B. Derivation of approximate, quadratic-bilinear flowfield model

In this supporting section, we present the derivation of a quadratic-bilinear model for the VIV flowfield, given the approximation of $F \approx \mathbb{I}$. This flowfield model structure and the approximation of the operators' adjacency-based sparsity comprise the basis for the presented sFOM inference approach.

The discretization of (9) in space with Finite Volumes, results to a set of ordinary differential equations for the internal DOFs of the fluid domain $\hat{\Omega}$ with the following structure:

$$\partial_t \hat{\mathbf{u}}_p = H_{FE}\left(\left(\hat{\mathbf{u}} - \partial_t \hat{\mathbf{d}}\right) \otimes \hat{\mathbf{u}}\right) + Q_{FE}\hat{\sigma}\left(\hat{\mathbf{u}}, \hat{p}\right), \tag{34}$$

where $\hat{\mathbf{u}}_p \in \mathcal{R}^{2n_p \times 1}$ and $\hat{\mathbf{u}} \in \mathcal{R}^{2n \times 1}$. n_p denotes the internal nodes of the 2D domain $\hat{\Omega}$ and $n - n_p$ would be the nodes on the domain boundary, computed through corresponding Dirichlet conditions in (4). The involved matrices can be considered sparse, originating from discretized differential operators. A Finite Element formulation with local basis functions yields similarly sparse matrices. By substituting $\hat{\sigma}\left(\hat{\mathbf{u}}, \hat{p}\right)$ for Newtonian fluids from (3), we get

$$\partial_t \hat{\mathbf{u}}_p = A_{FE}\hat{\mathbf{u}} + G_{FE}\hat{\mathbf{p}} + H_{FE}\left(\left(\hat{\mathbf{u}} - \partial_t \hat{\mathbf{d}}\right) \otimes \hat{\mathbf{u}}\right), \tag{35}$$

We note that (35) includes only equations for the internal velocity DOFs and not for the flow Dirichlet boundary conditions given in (4). A_{FE} encodes the viscous dissipation term. Through the Kronecker product, quadratic and bilinear terms are included, corresponding to the advection term of (9) and G_{FE} encodes the pressure gradient term.

At this point, the algebraic relation between pressure $\hat{\mathbf{p}}$ and velocity $\hat{\mathbf{u}}$ is inserted to (34). We first discretize the Poisson Eq. (10) in space, which leads to a quadratic bilinear structure

$$E_{PE}\hat{\mathbf{p}} = H_{PE}\left(\hat{\mathbf{u}} \otimes \hat{\mathbf{u}}\right) + K_{PE}\left(\partial_t \hat{\mathbf{d}} \otimes \hat{\mathbf{u}}\right). \tag{36}$$

Matrix E_{PE} is the discretized version of the negative Laplacian, and matrices H_{PE}, K_{PE} originate from the respective discretization of differential operators in the right-hand side of (10). We complement this set of discrete equations with the outlet ($x = l$) Neumann boundary condition of (4). This boundary condition introduces additional linear equations, such that the augmented system is

$$E_p\hat{\mathbf{p}} = A_p\hat{\mathbf{u}} + H_p\left(\hat{\mathbf{u}} \otimes \hat{\mathbf{u}}\right) + K_p\left(\partial_t \hat{\mathbf{d}} \otimes \hat{\mathbf{u}}\right). \tag{37}$$

where A_p originates from the outflow "do nothing" boundary condition. Matrices E_p, A_p, H_p, K_p are banded and sparse.

The inverse of E_p can be approximated by a band-dominated matrix [54], while the corresponding band can be reduced through several re-ordering methods, e.g. [55]. We thus assume that by substituting Eqs. (37) to (35), the resulting operators can be still approximated by sparse matrices, with non-zero elements only in positions corresponding to adjacent nodes of any given internal grid node and thus, any matrix row. The resulting structure is

$$\partial_t \hat{\mathbf{u}}_p = A_1\hat{\mathbf{u}} + H_1\left(\hat{\mathbf{u}} \otimes \hat{\mathbf{u}}\right) + K_1\left(\partial_t \hat{\mathbf{d}} \otimes \hat{\mathbf{u}}\right). \tag{38}$$

The grid deformation $\partial_t \hat{\mathbf{d}}$ is only dependent on $\partial_t \mathbf{d}_s$, for any linear ALE map (see (6)). Denoting the ALE map with A_L, we have

$$A_L \hat{\mathbf{d}} = \mathbf{d}_s - \mathbf{d}_s(t = 0) \tag{39}$$

Hence, we can substitute the above relation to the bilinear term of (38), by inverting A_L, using the same argumentation from [54]. We should note that for the currently employed ALE map, A_L is the discretized Laplace operator Λ (see (15)). At this point, we also discretize the time derivative $\partial_t \hat{\mathbf{u}}_p$ using an explicit Euler scheme. The discrete mapping of the velocity field from timestep k to $k+1$ would then be

$$\hat{\mathbf{u}}_p^{k+1} = A_e\hat{\mathbf{u}}^k + H_e\left(\hat{\mathbf{u}}^k \otimes \hat{\mathbf{u}}^k\right) + K_e\left(\partial_t \mathbf{d}_s^k \otimes \hat{\mathbf{u}}^k\right). \tag{40}$$

If an implicit Euler scheme is used, one more matrix inversion (see (38)) is required to isolate $\hat{\mathbf{u}}^{k+1}$. The corresponding structure is then

$$\hat{\mathbf{u}}_p^{k+1} = A_i\hat{\mathbf{u}}^k + H_i\left(\hat{\mathbf{u}}^{k+1} \otimes \hat{\mathbf{u}}^{k+1}\right) + K_i\left(\partial_t \mathbf{d}_s^{k+1} \otimes \hat{\mathbf{u}}^{k+1}\right). \tag{41}$$

At the inference level discussed in Section 3.4, no major difference was observed between the predictions of the inferred models with explicit (40) or implicit (41) formulations. We followed formulation (41), however both formulations require an implicit coupling with the solid dynamics Eqs. (1).

This coupling is introduced by the bilinear term as well as the kinematic boundary conditions at the FSI interface. We complement the system to include the Dirichlet conditions from (4), by adding $2n - 2n_p$ zero rows to the matrices of system (39) corresponding to DOFs at the domain boundary. For these DOFs, we introduce matrices L and B, with appropriate entries of value 1, such that the Dirichlet BCs at the FSI interface and the channel inlet are satisfied. The final, complete system of discrete-time equations is then given by

$$\begin{aligned}\hat{\mathbf{u}}^{k+1} = {} & A_f\hat{\mathbf{u}}^k + H_f\left(\hat{\mathbf{u}}^{k+1} \otimes \hat{\mathbf{u}}^{k+1}\right) + K_f\left(\partial_t \mathbf{d}_s^{k+1} \otimes \hat{\mathbf{u}}^{k+1}\right) \\ & + B\,\partial_t \mathbf{d}_s^{k+1} + L\,\mathbf{u}_{in}^{k+1},\end{aligned} \tag{42}$$

for the vector of velocity unknowns $\hat{\mathbf{u}} \in \mathcal{R}^{2n \times 1}$, where $\mathbf{u}_{in}$ is the vector of inlet velocity DOFs and $\partial_t \mathbf{d}_s$ is the 2×1 solid body velocity vector. Eq. (42) indicates that an implicit coupling between the fluid and solid dynamics at timestep $k+1$ is required. The numerical realization of this is analyzed in Section 3.7.

It remains to show the effect of subtracting a mean flowfield to the model structure. If the velocity field $\hat{\mathbf{u}}$ is decomposed to a mean flowfield $\overline{\mathbf{u}}$ and a time-varying component $\tilde{\mathbf{u}}(t)$ then we get

$$\hat{\mathbf{u}}(t) = \overline{\mathbf{u}} + \tilde{\mathbf{u}}(t) \tag{43}$$

and correspondingly

$$\partial_t \mathbf{d}_s(t) = \overline{\partial_t \mathbf{d}_s} + \partial_t \tilde{\mathbf{d}}(t). \tag{44}$$

Substituting $\overline{\mathbf{u}}$ with $\overline{\partial_t \mathbf{d}_s}$ to (38) and using (39), results to

$$0 = A_1\overline{\mathbf{u}} + H_1\left(\overline{\mathbf{u}} \otimes \overline{\mathbf{u}}\right) + K_1\left(\overline{\partial_t \mathbf{d}_s} \otimes \overline{\mathbf{u}}\right). \tag{45}$$

As a side note we observe that physically, $\overline{\mathbf{u}}$ should correspond to $\overline{\partial_t \mathbf{d}_s} = 0$ for a finite domain Ω. Substituting (43) to (38) results to

$$\partial_t \tilde{\mathbf{u}} = A_1'\tilde{\mathbf{u}} + B_1'\partial_t \tilde{\mathbf{d}} + H_1'\left(\tilde{\mathbf{u}} \otimes \tilde{\mathbf{u}}\right) + K_1'\left(\partial_t \tilde{\mathbf{d}} \otimes \tilde{\mathbf{u}}\right). \tag{46}$$

If $\overline{\mathbf{u}}$ and $\overline{\partial_t \mathbf{d}_s}$ are not the exact steady-state solution but only an approximation (e.g. a time-averaged flowfield), (45) will not be satisfied. This introduces a bias vector C to (47) such that

$$\partial_t \tilde{\mathbf{u}} = A_1'\tilde{\mathbf{u}} + B_1'\partial_t \tilde{\mathbf{d}} + H_1'\left(\tilde{\mathbf{u}} \otimes \tilde{\mathbf{u}}\right) + K_1'\left(\partial_t \tilde{\mathbf{d}} \otimes \tilde{\mathbf{u}}\right) + C. \tag{47}$$

By following the aforementioned time discretization and augmentation by the boundary conditions (subtracting the corresponding average values), we get the structure

$$\begin{aligned}\tilde{\mathbf{u}}^{k+1} = {} & A\tilde{\mathbf{u}}^k + H\left(\tilde{\mathbf{u}}^{k+1} \otimes \tilde{\mathbf{u}}^{k+1}\right) + K\left(\partial_t \tilde{\mathbf{d}}_s^{k+1} \otimes \tilde{\mathbf{u}}^{k+1}\right) \\ & + B\,\partial_t \tilde{\mathbf{d}}_s^{k+1} + L\,\tilde{\mathbf{u}}_{in}^{k+1} + C.\end{aligned} \tag{48}$$

References

[1] Sarpkaya T. A critical review of the intrinsic nature of vortex-induced vibrations. J Fluids Struct 2004;19:389–447. http://dx.doi.org/10.1016/j.jfluidstructs.2004.02.005.

[2] Williamson CHK, Govardhan R. Vortex-induced vibrations. Annu Rev Fluid Mech 2004;36:413–55. http://dx.doi.org/10.1146/annurev.fluid.36.050802.122128.

[3] Bearman PW. Understanding and predicting vortex-induced vibrations. J Fluid Mech 2009;634:1–4. http://dx.doi.org/10.1017/S0022112009990851.

[4] Kang Z, Yang C, Zhang C, Chang R, Zhai Y. Modification and application of low Reynolds number k– ϵ turbulence model to vortex-induced vibration at subcritical Reynolds number range. J Mar Sci Technol (Jpn) 2021;26:713–33. http://dx.doi.org/10.1007/s00773-020-00749-y.

[5] Govardhan R, Williamson CHK. Modes of vortex formation and frequency response of a freely vibrating cylinder. J Fluid Mech 2000;420:85–130. http://dx.doi.org/10.1017/S0022112000001233.

[6] Kang Y, Xiao W, Wang Q, Zhang D, Zhao J. Suppression of vortex-induced vibration by fairings on marine risers. J Ocean Univ China 2020;19:298–306. http://dx.doi.org/10.1007/s11802-020-4033-0.

[7] Carlson DW, Modarres-Sadeghi Y. Vortex-induced vibration of spar platforms for floating offshore wind turbines. Wind Energy 2018;21:1169–76. http://dx.doi.org/10.1002/we.2221.

[8] Jafari M, Hou F, Abdelkefi A. Wind-induced vibration of structural cables. Nonlinear Dynam 2020;100:351–421. http://dx.doi.org/10.1007/s11071-020-05541-6.

[9] Zheng M, Han D, Gao S, Wang J. Numerical investigation of bluff body for vortex induced vibration energy harvesting. Ocean Eng 2020;213:107–22. http://dx.doi.org/10.1016/j.oceaneng.2020.107624.

[10] Grouthier C, Michelin S, Bourguet R, Modarres-Sadeghi Y, de Langre E. On the efficiency of energy harvesting using vortex-induced vibrations of cables. J Fluids Struct 2014;49:427–40. http://dx.doi.org/10.1016/j.jfluidstructs.2014.05.004.

[11] Takizawa K, Tezduyar TE. Space-time fluid-structure interaction methods. Math Models Methods Appl Sci 2012;22. http://dx.doi.org/10.1142/S0218202512300013.

[12] Fernández MA, Gerbeau JF, Grandmont C. A projection semi-implicit scheme for the coupling of an elastic structure with an incompressible fluid. Internat J Numer Methods Engrg 2007;69:794–821. http://dx.doi.org/10.1002/nme.1792.

[13] Bazilevs Y, Takizawa K, Tezduyar TE. Challenges and directions in computational fluid-structure interaction. Math Models Methods Appl Sci 2013;23:215–21. http://dx.doi.org/10.1142/S0218202513400010.

[14] Richter T. Fluid-structure interactions models, analysis and finite elements. In: Fluid-structure interactions. Lecture notes in computational science and engineering, vol. 118, Springer; 2017.

[15] Lozovskiy A, Olshanskii MA, Vassilevski YV. Analysis and assessment of a monolithic FSI finite element method. Comput & Fluids 2019;179:277–88. http://dx.doi.org/10.1016/j.compfluid.2018.11.004.

[16] He T. Numerical solution techniques for fluid-structure interaction simulations: A brief review and discussion. Zhendong yu Chongji (J Vib Shock) 2018;37:184–90. http://dx.doi.org/10.13465/j.cnki.jvs.2018.04.028.

[17] Dowell EH, Hall KC. Modeling of fluid-structure interaction. Annu Rev Fluid Mech 2001;33:445–90. http://dx.doi.org/10.1146/annurev.fluid.33.1.445.

[18] Lorentzon J, Revstedt J. On stability and relaxation techniques for partitioned fluid-structure interaction simulations. Eng Rep 2022;4(10):e12514. http://dx.doi.org/10.1002/eng2.12514.

[19] Cai S, Mao Z, Wang Z, Yin M, Karniadakis GE. Physics-informed neural networks (PINNs) for fluid mechanics: a review. Acta Mech Sin/lixue xuebao 2021;37:1727–38. http://dx.doi.org/10.1007/s10409-021-01148-1.

[20] Schmid PJ, Li L, Juniper MP, Pust O. Applications of the dynamic mode decomposition. Theor. Comput. Fluid Dyn. 2011;25:249–59. http://dx.doi.org/10.1007/s00162-010-0203-9.

[21] Peherstorfer B, Willcox KE. Data-driven operator inference for nonintrusive projection-based model reduction. Comput Methods Appl Mech Engrg 2016;306:196–215. http://dx.doi.org/10.1016/j.cma.2016.03.025.

[22] Gosea IV, Poussot-Vassal C, Antoulas AC. Data-driven modeling and control of large-scale dynamical systems in the Loewner framework: Methodology and applications. Handb Numer Anal 2022;23:499–530. http://dx.doi.org/10.1016/bs.hna.2021.12.015.

[23] Liberge E, Hamdouni A. Reduced order modelling method via proper orthogonal decomposition (POD) for flow around an oscillating cylinder. J Fluids Struct 2010;26:292–311. http://dx.doi.org/10.1016/j.jfluidstructs.2009.10.006.

[24] Riches G, Martinuzzi R, Morton C. Proper orthogonal decomposition analysis of a circular cylinder undergoing vortex-induced vibrations. Phys Fluids 2018;30:105103. http://dx.doi.org/10.1063/1.5046090.

[25] Nonino M, Ballarin F, Rozza G. A monolithic and a partitioned, reduced basis method for fluid–structure interaction problems. Fluids 2021;6:229–64. http://dx.doi.org/10.3390/fluids6060229.

[26] Benner P, Richter T, Weinhandl R. A low-rank approach for nonlinear parameter-dependent fluid-structure interaction problems. Lecture notes in computational science and engineering, vol. 139, 2021, p. 1157–65. http://dx.doi.org/10.1007/978-3-030-55874-1_115.

[27] Lieu T, Farhat C, Lesoinne M. POD-based aeroelastic analysis of a complete F-16 configuration: Rom adaptation and demonstration. In: Collection of technical papers - AIAA/aSME/ASCE/AHS/aSC structures, structural dynamics and materials conference, vol. 9. 2005, p. 6103–18. http://dx.doi.org/10.2514/6.2005-2295.

[28] Poussot-Vassal C, Quero D, Vuillemin P. Data-driven approximation of a high fidelity gust-oriented flexible aircraft dynamical model. 51, 2018, p. 559–64. http://dx.doi.org/10.1016/j.ifacol.2018.03.094,

[29] Dai Y, Rong H, Wu Y, Yang C, Xu Y. Stall flutter prediction based on multi-layer GRU neural network. Chin J Aeronaut 2023;36:75–90. http://dx.doi.org/10.1016/j.cja.2022.07.011.

[30] Prasad AK. Particle image velocimetry. Current Sci 2000. http://dx.doi.org/10.1201/b19031-55.

[31] Zastrow BG, Chaudhuri A, Willcox KE, Ashley AS, Henson MC. Data-driven model reduction via operator inference for coupled aeroelastic flutter. In: AIAA SciTech 2023 forum. 2023, http://dx.doi.org/10.2514/6.2023-0330.

[32] Xiao D, Yang P, Fang F, Xiang J, Pain CC, Navon IM. Non-intrusive reduced order modelling of fluid-structure interactions. Comput Methods Appl Mech Engrg 2016;303:35–54. http://dx.doi.org/10.1016/j.cma.2015.12.029.

[33] Yao W, Jaiman RK. Model reduction and mechanism for the vortex-induced vibrations of bluff bodies. J Fluid Mech 2017;827:357–93. http://dx.doi.org/10.1017/jfm.2017.525.

[34] Navrose, Yogeswaran V, Sen S, Mittal S. Free vibrations of an elliptic cylinder at low Reynolds numbers. J Fluids Struct 2014;51:55–67. http://dx.doi.org/10.1016/j.jfluidstructs.2014.07.012.

[35] Prasanth TK, Mittal S. Vortex-induced vibration of two circular cylinders at low Reynolds number. J Fluids Struct 2009;25:731–41. http://dx.doi.org/10.1016/j.jfluidstructs.2008.12.002.

[36] Sarna N, Benner P. Learning reduced order models from data for hyperbolic PDEs. 2021, http://dx.doi.org/10.48550/arXiv.2109.06156, arXiv:2109.06156.

[37] Benner P, Goyal P, Heiland J, Pontes Duff I. Operator inference and physics-informed learning of low-dimensional models for incompressible flows. Electron Trans Numer Anal 2021;56:28–51. http://dx.doi.org/10.1553/ETNA_VOL56S28.

[38] Mendez MA, Raiola M, Masullo A, Discetti S, Ianiro A, Theunissen R, et al. POD-based background removal for particle image velocimetry. Exp Therm Fluid Sci 2017;80:181–92. http://dx.doi.org/10.1016/j.expthermflusci.2016.08.021.

[39] Baddoo PJ, Herrmann B, McKeon BJ, Kutz NJ, Brunton SL. Physics-informed dynamic mode decomposition. Proc R Soc Lond Ser A Math Phys Eng Sci 2023. http://dx.doi.org/10.1098/rspa.2022.0576.

[40] Schumann Y, Neumann P. On linear models for discrete operator inference in time dependent problems. J Comput Appl Math 2023;425:115022. http://dx.doi.org/10.1016/j.cam.2022.115022.

[41] Schumann Y, Neumann P. Towards data-driven inference of stencils for discrete differential operators. In: Proceedings of the platform for advanced scientific computing conference. 2022, http://dx.doi.org/10.1145/3539781.3539787.

[42] Schaeffer H, Tran G, Ward R. Extracting sparse high-dimensional dynamics from limited data. SIAM J Appl Math 2018. http://dx.doi.org/10.1137/18M116798X.

[43] Swischuk R, Kramer B, Huang C, Willcox KE. Learning physics-based reduced-order models for a single-injector combustion process. AIAA J 2020;58:2658–72. http://dx.doi.org/10.2514/1.J058943.

[44] McQuarrie SA, Huang C, Willcox KE. Data-driven reduced-order models via regularised operator inference for a single-injector combustion process. J R Soc New Zealand 2021;51:194–211. http://dx.doi.org/10.1080/03036758.2020.1863237.

[45] Hansen PC. The L-curve and its use in the numerical treatment of inverse problems. In: Johnston P, editor. Computational inverse problems in electrocardiology. Advances in computational bioengineering, vol. 5, 2000, p. 119–42, doi: 10.1.1.33.6040.

[46] Anttonen JSR, King PI, Beran PS. POD-based reduced-order models with deforming grids. Math Comput Modelling 2003;69:794–821. http://dx.doi.org/10.1016/S0895-7177(03)90005-7.

[47] Richter T, Wick T. Finite elements for fluid-structure interaction in ALE and fully Eulerian coordinates. Comput Methods Appl Mech Engrg 2010;199:2633–42. http://dx.doi.org/10.1016/j.cma.2010.04.016.

[48] Cori JF, Etienne S, Garon A, Pelletier D. High-order implicit Runge-Kutta time integrators for fluid-structure interactions. Internat J Numer Methods Fluids 2015;78:385–412. http://dx.doi.org/10.1002/fld.4020.

[49] Becker R, Braack M, Meidner D, Richter T, Vexler B. The finite element toolkit Gascoigne (v1.01). Zenodo; 2021, http://dx.doi.org/10.5281/zenodo.5574968.

[50] Engwirda D. Locally-optimal Delaunay-refinement and optimisation-based mesh generation. [Ph.D thesis], School of Mathematics and Statistics, The University of Sydney, Australia; September 2014.

[51] Noack BR, Afanasiev K, Morzyński M, Tadmor G, Thiele F. A hierarchy of low-dimensional models for the transient and post-transient cylinder wake. J Fluid Mech 2003;497:335–63. http://dx.doi.org/10.1017/S0022112003006694.

[52] Khalak A, Williamson CHK. Motions, forces and mode transitions in Vortex-Induced Vibrations at low mass-damping. J Fluids Struct 1999;13:813–51. http://dx.doi.org/10.1006/jfls.1999.0236.

[53] Shen L, Chan ES, Wei Y. Beating motion of a circular cylinder in vortex-induced vibrations. Fluid Dyn Res 2018;50(2). http://dx.doi.org/10.1088/1873-7005/aa9a0d.

[54] Bickel P, Lindner M. Approximating the inverse of banded matrices by banded matrices with applications to probability and statistics. Theory Probab Appl 2012;56:1–20. http://dx.doi.org/10.1137/S0040585X97985224.

[55] Reid JK, Scott JA. Reducing the total bandwidth of a sparse unsymmetric matrix. SIAM J Matrix Anal Appl 2006;28:805–21. http://dx.doi.org/10.1137/050629938.